Research Square

Preprints are preliminary reports that have not undergone peer review.
They should not be considered conclusive, used to inform clinical practice,
or referenced by the media as validated information.

Carbon remodeling aids marsh adaptation and resilience in Typha (Cattails)

Joseph Noel

noel@salk.edu

Salk Institute for Biological Studies https://orcid.org/0000-0002-1277-0331

Shrikaar Kambhampati

Salk Institute for Biological Studies https://orcid.org/0000-0003-1582-0733

Leonardo Andrade

Salk Institute for Biological Studies

Bradley Abramson

The Salk Institute for Biological Studies

Karl Wessendorf-Rodriguez

Salk Institute for Biological Studies

Anna De Angelis

Salk Institute for Biological Studies

Suzanne Thomas

Salk Institute for Biological Studies

Justin Pacheco

Salk Institute for Biological Studies

James La Clair

Salk Institute for Biological Studies

Carl Procko

Louisiana State University

Rebecca Re

Salk Institute for Biological Studies https://orcid.org/0000-0001-7004-4971

Jiahong Zhou

Donald Danforth Plant Science Center

Kelly Colt

Salk Institute for Biological Studies

Nicholas Allsing

Salk Institute for Biological Studies https://orcid.org/0000-0002-1145-1646

Nolan Hartwick

Rutgers University

David McNear

University of Kentucky
Doug Allen
Donald Danforth Plant Science Center https://orcid.org/0000-0001-8599-8946
Todd Michael
Salk Institute for Biological Studies https://orcid.org/0000-0001-6272-2875
Christian Metallo
Salk Institute for Biological Studies

Biological Sciences - Article

Keywords:

Posted Date: August 20th, 2026

DOI: https://doi.org/10.21203/rs.3.rs-10607151/v1

License: This work is licensed under a Creative Commons Attribution 4.0 International License.
Read Full License

Additional Declarations: Yes there is potential Competing Interest. T.P.M. and J.P.N. are co-founders of Cquesta, Inc., a company that works on crop root growth and carbon sequestration. All other authors declare no competing interests.

Abstract

Wetland plants contribute to long term carbon storage, shoreline stabilization, bioremediation, and flood protection, yet the traits that allow them to thrive in oxygen-poor sediments remain poorly understood 1,2. Identifying these traits is increasingly important as many crops are vulnerable to waterlogging, hypoxia and unstable hydrology. Therefore, wetland plants can reveal new strategies to develop more resilient crops 3. Typha domingensis (Southern Cattail) is a dominant marsh species with exceptional tolerance for inundation, but its survival strategies have not been fully resolved 4–6. Here we show that T. domingensis employs clonal propagation, convective internal gas flow, flexible carbon metabolism and selective root barriers with unusual suberin chemistry. By combining anatomy, cell wall chemistry, genomics, developmental multi-omics and isotope tracing, we demonstrate that barrier formation is supported by coordinated shifts in phenylpropanoid metabolism, fatty-acid elongation and shoot-to-root carbon transport, including a prominent contribution of serine-linked one-carbon metabolism 7. Hypoxia suppresses bulk lipid biosynthesis while preserving the outer root barrier, revealing selective remodeling rather than simple barrier induction. These findings establish T. domingensis as a mechanistically tractable system for understanding how plants balance aeration, barrier formation and carbon allocation in their roots. More broadly, they identify wetland plants as a rich source of structural and metabolic design principles for engineering crop resilience in a warming world 3.

Main

Wetlands are among the most productive and consequential ecosystems on Earth, buffering floods, stabilizing shorelines, improving water quality and storing large carbon stocks in waterlogged soils [8–11]. When wetlands are degraded, these long-lived carbon stores are rapidly reactivated, releasing CO_2 and methane that weaken climate and coastal resilience [2,9,11]. Much of this resilience depends on specialized plants, which must sustain growth in flooded, oxygen-poor, brackish and chemically reduced soils, conditions that increasingly threaten agriculture [3]. Therefore, these plants represent an underused reservoir of traits for climate-resilient crops. However, the most relevant traits are unlikely to be identified by species inventories alone. What is needed is a combination of genetic and mechanistic understandings of how anatomical structures, protective barriers and carbon metabolism are coordinated to maintain root function in chronically waterlogged soils.

Typha (Cattails) is a useful plant phyla for addressing these questions because it is widespread globally, fast-growing and often dominant in freshwater and slightly brackish marshes [4]. Among North American species, *Typha domingensis* (Southern Cattail) is especially informative as it occupies warmer habitats, tolerates deeper inundation, and persists in brackish and high-pH environments [5,6]. Its clonal rhizome network also supports rapid colonization and strong belowground persistence [4]. This ecology makes *T. domingensis* not simply a wetland inhabitant, but a marsh-building foundation species whose survival strategy warrants mechanistic study.

The success of *T. domingensis* suggests that wetland adaptation is an emergent property of linked structural and metabolic traits. Aerenchyma in leaves, rhizomes and roots sustains internal pressurization and convective gas flow, but active gas transport alone cannot explain persistence in reducing soils. Root survival also depends on barrier tissues that regulate oxygen leakage, solute entry and water balance. Suberin, a hydrophobic and chemically complex polyester, is central to this interface. Suberin assembly integrates fatty-acid metabolism, phenylpropanoid chemistry and cell-wall formation into a protective apoplastic barrier to radial oxygen loss and solute penetration [12]. Despite its importance for wetland specialization, we know little about how suberin is deployed in dominant marsh plants, how its chemistry differs from that of terrestrial plants, and how its biosynthesis is supported by carbon allocation under low-oxygen conditions.

Here we establish *T. domingensis* as a model wetland species to define how marsh-adaptive traits are organized from anatomy to metabolism. We first show that its clonal axis couples continuous internal aeration from shoot to selective root barriers. We then demonstrate that its root barrier is chemically distinct from those of crops such as rice (*Oryza sativa*), soybean (*Glycine max*) and wheat (*Triticum aestivum*), with unusual enrichment in very-long-chain (VLC) suberin aliphatic carbon chains. To support mechanistic analysis, we generate a chromosome-resolved genome and a developmental anatomical and transcriptomic series spanning the onset of barrier deposition. Finally stable-isotope tracing with $^{13}CO_2$ and [U-^{13}C]glucose reveal how shoot-derived carbon, serine metabolism, and lipid-flux remodeling are key to barrier formation and hypoxia tolerance. The combined results establish *T. domingensis* as a tractable system for understanding wetland adaptation and provide a rich source of transferable traits that will enable the future development of more resilient crops.

Typha anatomy supports marsh adaptation

Whole-plant imaging and serial sections show that *T. domingensis* is organized as a connected clonal axis in which ramets are linked by rhizomes and by a continuous lacunar system extending from rhizome and stem base into the leaf and root suggesting a through-plant gas network (Fig. 1a–c). Earlier work on *Typha* reported humidity-driven pressurized throughflow: air enters middle-aged leaves, flows convectively down the leaf lacunae into the rhizome, and is vented through older leaves or horizontal rhizomes to neighboring shoots [13]. Rice also contains extensive aerenchyma, but live imaging indicates that long-distance gas transport in rice is predominantly diffusion-driven, following gas partial-pressure gradients from emerged leaves to submerged organs [14]. Thus, the architecture in Fig. 1 is consistent with a stand-level ventilation network rather than a purely diffusion-based axis.

Our root sections further show a multiseriate exodermis, with strong Fluorol Yellow signals in the outer cell layers and TEM-visible suberin lamellae in both exodermal and endodermal cell walls (Fig. 1d-f). These data extend earlier physiological studies showing that *T. domingensis* can sustain substantial subapical radial oxygen loss (ROL) while maintaining low alcohol dehydrogenase activity and ethanol accumulation, consistent with oxygen leakage from a well-aerated plant rather than internal oxygen deficit [15,16]. This differs from rice where outer root suberization forms a tight basal barrier to ROL that

conserves oxygen for the apex [17,18]. The coexistence of multilayered exodermal suberization and substantial oxygen leakage in *T. domingensis* suggests selective rather than absolute barriers. The outer cell wall likely restricts solute entry and oxygen loss at the soil interface, while still permitting the rhizosphere oxidation that accompanies marsh survival. The weaker Fluorol Yellow signal in the endodermis (Supplemental Fig S1), despite clear lamellae by TEM, further suggests that exodermal and endodermal suberin
differ in abundance and possibly composition [19,20].

Leaf anatomy complements this organization. Our sections show that chlorophyll-bearing palisade parenchyma is restricted to the blade margins, whereas the leaf interior is dominated by large lacunae and non-palisade mesophyll (Fig. 1c). Earlier work in *Typha latifolia* found that aerenchyma CO_2 can far exceed atmospheric levels by more than an order of magnitude and can be reassimilated by internal leaf surfaces [21,22] thus retaining a high photosynthetic capacity, despite extensive air spaces [23.]. The anatomy documented here supports a division of labor in which the leaf interior prioritizes long-distance gas movement and the marginal chlorenchyma remains positioned for both light capture and reassimilation of internally transported CO_2, similar to synergistic metabolism previously described for mixotrophic systems [24,25]. Combined, these observations define a marsh-adapted axis that integrates clonal propagation, internal gas pressurization, and selective outer root barriers that enable efficient carbon use across the plant.

Typha builds a distinctive suberin barrier

Next, we asked whether this anatomical complexity is supported by distinctive cell wall chemistry. The ^{13}C Cross Polarization – Magic Angle Spinning solid-state Nuclear Magnetic Resonance (CP-MAS ssNMR) spectrum of *Typha* roots resolved the carbonyl, aryl, O-/N-alkyl and alkyl regions, with a significant amount of long chain fatty acids as shown by the methylene signals across the 28-35 ppm alkyl region of the NMR spectrum (Fig. 2a). Similar methylene environments have been described in cork suberin [26], suggesting that *Typha* roots contain a strongly aliphatic cell wall component. Comparative Direct Polarization (DP) MAS ssNMR spectra showed that *Typha* and soybean were the most alkyl-enriched roots, whereas *Typha* and waterlogged rice carried the strongest aryl signals, with wheat remaining the most O/N-alkyl-dominated cereal (Fig. 2b,c, Supplemental table S2) largely attributed to enrichment in sugars and cellulose, while the alkyl-to-O-/N-alkyl ratio increases as tissues become more aliphatic-rich relative to carbohydrate-rich material [25,26].

Gas Chromatography - Mass Spectrometry (GC–MS) analyses of depolymerized cell wall residues also supported these interpretations. Soybean served as a high-suberin-containing dicot benchmark and matched previous reports of suberin polymer dominated by C18:1-derived ω-hydroxy and α,ω-diacids [27]. Rice provided a contrasting monocot benchmark because waterlogging induces an exodermal barrier enriched in ferulate- and coumarate-containing suberin [18,28]. While some rice VLCFAs (>24C) were detected as hydrolyzed suberin monomers, the majority that were induced under waterlogging remained

in the extractable lipids (Supplemental Fig S2, Supplemental table S3). Against these crop patterns, *Typha* stood out not because it accumulated more of the same monomers, but because a substantial fraction of its aliphatic polymer occurred as VLCFAs above C24, with abundant C24–C30 monomers recovered directly from the suberin residue (Fig. 2d, Supplemental table S4). Wheat occupied the opposite end of the comparison, lacking both *Typha*-like VLCFA enrichment and the larger total aliphatic pool.

Aromatic features were equally distinctive in *Typha* with a strong aryl signal in the NMR spectra (Fig. 2b), together with abundant *p*-coumarate and ferulate detection by GC-MS analysis (Fig. 2d), indicating a hydroxycinnamate-rich cell wall chemistry that is closer to monocot barrier tissues than to soybean. Yet, relative to the other three species, *Typha* contained substantially more aliphatic suberin (Fig. 2e, Supplemental table S5), comprised of VLCFAs, primary alcohols and ω-hydroxy acids. The *Typha* barrier composition advantage lies in its beneficial attributes compared to other crops: a soybean-like abundance of aliphatics and a rice-like aromatic reinforcement.

This chemistry, together with the multiseriate exodermis and dual exodermal/endodermal lamellae described in Fig. 1, argues that the *Typha* marsh barrier is chemically stratified as well as anatomically layered. Because barrier function depends on composition and cell wall microstructure rather than bulk amount alone [19,28], we interpret Fig. 2 primarily as evidence for an exceptionally lipidized and chemically reinforced barrier system, rather than as a direct proxy for impermeability. The enrichment of C24–C30 aliphatics also has ecological implications. Suberin monomers are widely used as biomarkers of root-derived carbon in soils. Recent field measurements show that suberin can contribute more than cutin to bulk soil organic carbon stocks [29,30], scales positively with root biomass [30], and persists long-term depending on both chemistry and soil context [31]. The unusually VLCFA-rich suberin of *T. domingensis* is therefore consistent with a chemistry well suited to both wetland root protection and long-term carbon retention in marsh soils. *Typha* thus provides a rare opportunity to study suberin in a species that is simultaneously barrier-rich, developmentally tractable, and ecologically central to carbon-storing wetlands.

Typha pangenome maps wetland-adaptive evolution

Recent genomes of *T. latifolia*, *T. angustifolia*, and *T. minima*, together with population genomic evidence of recurrent isolation, secondary contact and hybridization, show that *Typha* genomes are compact but evolutionarily dynamic [32–35] . Given the broad ecological distribution and dispersal capacity of Typha, we asked whether populations from distinct habits retain genomic signatures of local adaptation. To address this, we generated a reference-quality chromosome-scale genome for *T. domingensis* together with chromosome-scale draft genomes from both *T. domingensis* and *T. latifolia* populations spanning ponds, beaches, lagoons, bayous and canyons from three distinct geographies, enabling construction of a *Typha* pangenome (Supplemental Fig. 3a; Supplemental Table S6).

Pairwise k-mer distances separated genomes by both species identity and geographic origin (Supplemental Fig. 3a) indicating that genome-wide variation reflects both divergence between *T. latifolia* and *T. domingensis* and regional structuring within each lineage. Because k-mer distances capture sequence variation across both coding and non-coding regions without reference genome bias, this pattern suggests that local selective pressures and restricted gene flow have contributed to shaping genomic diversity across North American *Typha* populations. The pangenome further revealed extensive dispensable genome (Supplemental Fig. 3b); 43.5 Mb of core sequence was shared among all genomes, whereas 47.0 Mb of k-mers were unique to *T. domingensis* and 35.1 Mb were unique to *T. latifolia*. Thus lineage-specific sequence is nearly as abundant as the shared core, consistent with substantial structural, transposon, copy-number, and gene presence-absence variation that may contribute to local marsh adaptation.

Comparative genomic analyses across 24 angiosperm proteomes, using OrthoFinder, produced 110,446 orthogroups, of which 3,991 contained at least one gene from every species (Supplemental Table S7). The rooted species tree placed *Typha* sister to *Ananas comosus* (pineapple) within Poales but outside the grass clade, consistent with the shared σ (sigma) and τ (tau) whole-genome duplication history mapped to ancestral monocot nodes (Fig 3a). *T. domingensis* (TD08) and *T. latifolia* (TL01) contributed 23,214 and 20,755 proteins respectively, all assigned to orthogroups. The two *Typha* species shared 7,257 orthogroups, compared with 7,215 shared between *T. domingensis* and *Ananas comosus* and 6,911 between *T. latifolia* and *Ananas comosus*. CAFE5 analysis identified 1,135 families with significant expansion or contraction ($p < 0.05$; $\lambda = 1.35$, $-\ln L = 411{,}852$). Among these significant families, *T. latifolia* showed 76 expansions and 404 contractions, while *T. domingensis* showed 225 expansions and 238 contractions. OrthoPos comparative profiling identified 92 orthogroups with significant copy-number differences between *Typha* and three *Oryza* species across eight pairwise and grouped comparisons, with 15 orthogroups significant in all eight comparisons.

GO enrichment analysis with five GO annotated species (*Arabidopsis thaliana*, *Glycine max*, *Oryza glaberrima*, *Oryza nivara*, and *Triticum aestivum*) identified significant GO terms (FDR < 0.05) for 12,169 orthogroups (Supplemental Table S8). Among the 75 orthogroups with significant *Typha* copy-number expansion in the OrthoPos comp analysis (TL or TD vs. grouped *Oryza*), 27 were annotated. The most strongly enriched terms included serine-type endopeptidase activity (GO:0004252), peroxidase activity (GO:0004601), response to oxidative stress (GO:0006979), heme binding (GO:0020037), extracellular region (GO:0005576), and plant-type cell (GO:0009505). These results collectively indicate enrichment of extracellular peroxidase activity, oxidative-stress responses, proteolysis (GO:0006508), and cell wall-associated functions among *Typha*-expanded orthogroups. Additional enriched terms included hydrogen peroxide catabolic process (GO:0042744), defense response (GO:0006950), cell wall organization (GO:0071555), and apoplast (GO:0048046), further reinforcing the association with cell wall remodeling and extracellular defense. Together, these functional enrichments are consistent with the ecological niche of *Typha* as a wetland macrophyte, where robust oxidative-stress tolerance, cell wall remodeling, pathogen defense, and specialized metabolism likely contribute to its competitive success in flooded, redox-variable environments. Collectively, the chromosome-scale genome and pangenome provide a

framework for studying wetland adaptation and for developmental, functional and metabolic analyses of suberin biology that follow.

Developmental onset of suberin assembly

To capture suberin metabolism during barrier formation rather than after its completion, we established a sterile plate-grown developmental series and harvested seedlings at 3, 4, and 5 weeks. Root diameter increased progressively across this window (Fig. 4a) and ultrastructural analysis showed that this interval spans the onset of lamellae deposition. No suberin lamellae were detected at 3 weeks, whereas both exodermal and endodermal lamellae were evident by 4 weeks and remained prominent at 5 weeks, with representative 5-week ultrastructure shown in Fig. 4b. This developmental series therefore captures the transition from an unsuberized juvenile root (Supplemental Fig S4) to a suberizing root and provides an experimentally tractable stage for mechanistic analysis of suberin assembly.

RNA sequencing (RNA-seq) confirmed a root-localized suberin program. Genes encoding the suberin associated enzymes KCS4-like, CYP86B1, HHT1/ASFT and GPAT4 all increased across the 3- to 5-week series in roots, but not in shoots (Fig. 4c, Supplemental table S9). These genes correspond to core steps of suberin biosynthesis: KCS enzymes extend acyl chains into the VLCFA range, CYP86B1 catalyzes ω-hydroxylation of long-chain precursors [36], ASFT mediates the transfer of feruloyl groups onto aliphatic intermediates [37], and GPAT family acyltransferases are central to root suberization [38]. Notably, recent work shows that the GPAT4/6/8 clade participates in developmentally regulated root suberization, whereas GPAT5/7 contributes more strongly to ABA-induced suberization [39], making the induction of a *Typha* GPAT4 orthologue consistent with a developmental barrier program rather than stress-only deposition.

Global differential expression reinforced this interpretation. The 5-week versus 3-week comparison identified induction of secondary cell wall and aromatic pathway regulators including NST1 and MYB85, alongside barrier-associated lipid genes such as KCS4, GPAT1 and CYP86B1 (Fig. 4d, Supplemental table S10). In Arabidopsis, NST1/NST3 and MYB85 regulate secondary cell wall formation and phenylalanine/lignin biosynthesis [40,41]. The same comparison also highlighted COPT1, WRKY22 and a phytoglobin-like GLB3, linking barrier formation to metal ion homeostasis and flood-response signaling [42,43]. These changes indicate that the onset of suberization in *Typha* is not an isolated lipid-polymer program, but part of a broader developmental stage in which secondary cell wall assembly, aromatic metabolism and environmental acclimation are co-activated.

The lipidome also shifted markedly as suberin accumulated. At 5 weeks, the dominant lipid classes were MGDG, PI, DGDG, DAG, PE and PC, indicating substantial contributions from plastid and extraplastid membranes (Fig. 4e, Supplemental table S11). However, across development most lipid classes declined on a fresh-weight basis (Fig. 4f, Supplemental table S12, S13), even as barrier-associated transcripts increased, suggesting that root maturation involves reallocation of fatty acids away from bulk membrane pools during lamellae assembly. The one exception was PI, which increased transiently at 4 weeks

before decreasing at 5 weeks. Because phosphoinositides are tightly linked to membrane trafficking and cell surface remodeling, this transient PI enrichment may reflect a burst of trafficking associated with lamellae assembly [44].

Soluble metabolite content changed in parallel. Most measured metabolites in the roots declined from 3 to 5 weeks across amino acids, organic acids, carbohydrates, pentose-phosphate intermediates, nucleotide metabolism, and nicotinate derivatives (Fig. 4g, Supplemental table S14). Because these values are normalized to fresh weight, the broad decrease is consistent with a developmental transition from a metabolite-rich juvenile root to a thicker, more structurally invested organ in which carbon is increasingly committed to cell wall, barrier and storage functions. Integrated transcript–metabolite analysis supported that view by highlighting phenylpropanoid biosynthesis, starch and sucrose metabolism, fatty acid elongation, glycerolipid metabolism, Gly/Ser/Thr metabolism and cutin, suberin and wax biosynthesis as the most impacted pathways (Fig. 4h). This integrated signature is important because it links the aromatic and aliphatic arms of the barrier in the same developmental window and points to simultaneous provisioning of carbon skeletons, reducing power and cell wall-building substrates.

The prominence of phenylpropanoid metabolism aligns with the hydroxycinnamate-rich barrier chemistry described above, whereas starch/sucrose metabolism and fatty acid elongation point to coordinated provisioning of carbohydrate and lipid precursors. The enrichment of “carbon fixation and Calvin cycle” terms is best interpreted cautiously as roots contain non-green plastids that can differentiate into starch-accumulating amyloplast-like states [45,46], and several enzymes annotated in Calvin-cycle maps also function in heterotrophic plastid metabolism [47]. We therefore interpret this signature as plastid and central-carbon remodeling in a non-photosynthetic root, rather than evidence for a canonical photosynthetic Calvin cycle. Together, Fig. 4 establishes a defined developmental system in which suberin deposition is anatomically visible, transcriptionally activated and metabolically coordinated [12,48]

Shoot carbon supports root suberization

To move beyond static metabolite pools and directly resolve carbon flow during barrier formation, we exposed 5-week-old *T. domingensis* seedlings to a humidified atmosphere containing $^{13}CO_2$ at 420 ppm over a 24-h light–dark cycle and monitored isotopic enrichment in shoots and roots (Fig. 5a). Roots of seedlings were maintained in ½ MS medium with no carbon source and $^{15}NO_3$ as sole nitrogen source. Arabidopsis seedlings were labelled in parallel as a photoautotrophic reference, following the same general logic used in Arabidopsis $^{13}CO_2$ labelling studies that benchmark Calvin-cycle and downstream fluxes in intact rosettes [49].

In the shoot, Calvin-cycle intermediates and immediate products of carbon assimilation, including G6P, S7P and sucrose, increased steadily and plateaued at only ~30% enrichment after 12 hours of labeling, and serine showed a similar partial-labelling behavior (Fig. 5b). This is notably lower than expected for a fully autotrophic system and instead points to dilution by pre-existing unlabeled carbon. Recent

$^{13}CO_2$ flux studies in Arabidopsis and Camelina show that incomplete labelling of Calvin-cycle intermediates can arise from reimport of carbon from cytosolic and vacuolar sugar pools and from recycling of stored carbohydrates through the G6P shunt, rather than from direct fixation alone [50]. The partial plateau in *Typha* is therefore consistent with a metabolically mixed system in which newly fixed carbon is continuously diluted by remobilized internal reserves, such as sucrose. Alternatively, this could also reflect substantial starch pools measured in both shoot and root that may partially turnover during the day (Supplemental Fig
S5a). Relative to the near-complete Calvin-cycle labeling typically expected from autotrophic leaves under similar protocols [49] that served as a control (Supplemental Fig S5b), the data suggest a more mixotrophic or synergistic carbon economy in 5-week *Typha* seedlings.

We next used SIMPEL to organize the root time-course data into precursor–product relationships based on enrichment kinetics (Fig. 5c). SIMPEL was developed specifically to interpret kinetic isotope-enriched metabolomics datasets and includes clustering tools that distinguish rapidly labelled precursors from slower downstream products [51]. In this analysis with >100 labeled small molecule measurements (Supplemental table S15), sucrose formed a single fast-labelling cluster, identifying it as the dominant imported carbon source to the root. A second cluster contained serine together with glutamine, asparagine, citrate and 2-oxoglutarate, consistent with entry of imported carbon into central root metabolism and nitrogen assimilation (Supplemental Fig S5c). The separation of sucrose from the more slowly labelled amino-acid/TCA cluster therefore indicates that recently fixed carbon reaches the suberizing root primarily as shoot-derived sucrose.

Serine, however, revealed an additional level of organization. In roots, the serine isotopologue pattern showed C_1N_0 enrichment occurred before C_0N_1, whereas phosphoserine labelled first as C_0N_1 (Fig. 5d,e). If root serine enriched predominantly through local phosphorylated serine biosynthesis (PPSB), phosphoserine and serine would be expected to show more similar early isotopologue ordering. Instead, the observed sequence is more consistent with substantial import of one-carbon-labeled serine from the shoot. This interpretation is strengthened by the transcript data, where the photorespiratory/glycolate-pathway for serine biosynthesis (GPSB) genes were far more abundant than the PPSB genes in 5-week seedlings (Fig. 5f). This observation is biologically plausible because plants synthesize serine through both PPSB and the photorespiratory glycolate pathway [52,53]. Isotopically non-stationary flux analysis in Arabidopsis has shown that a substantial fraction of photorespiratory carbon can be exported as serine, which serves as the main conduit linking photorespiration to one-carbon metabolism [7,54]. A large demand for serine-linked one-carbon units is in accord with ferulate synthesis that depends on S-adenosylmethionine-dependent methyl transfer [55], to support the unusually high ferulate content of *Typha* root barriers (Fig. 2). Our data therefore support a model in which shoot photorespiration supplies serine to roots to help sustain hydroxycinnamate-rich suberin and lignin formation, similar to previous reports [7,56]. A local root contribution cannot be excluded, because heterotrophic tissues can express photorespiratory components and even divergent non-photosynthetic Rubisco small subunits [57]. As such, transcripts for both the large and small subunit of Rubisco as well as GPSB genes are abundant in

roots of Typha (Supplemental Fig S5d). Nonetheless, Fig. 5 identifies newly fixed sucrose as the principal carbon input to suberizing roots and implicates serine as a key intermediate linking photorespiration to root barrier biogenesis.

Hypoxia remodels lipid and suberin flux

Using [U-^{13}C]glucose and isotopomer spectral analysis (ISA) [58], we resolved the production of fatty acids into *de novo* plastidial synthesis and ER-based elongation, based on C16 chain plastidial assembly and C24 chains representing VLC elongation. The ISA fit required three precursor pools: two plastidial lipogenic acetyl-CoA pools (AcCoA-PL1 and AcCoA-PL2) feeding C16/C18 synthesis, and one ER-associated acetyl-CoA pool supplying carbon for elongation to C24 chains (Supplemental table S17). The two plastidial pools were consistently required across the span of development (Supplemental table S18), indicating that fatty acid synthesis receives multiple supplies of acetyl-CoA and does not behave as a single well-mixed precursor pool in *Typha* roots. This heterogeneity could reflect distinct cell types, subplastidial states or unequal access of neighboring tissues to imported carbon, and it highlights one of the advantages of *Typha* as a model for dissecting root metabolic compartmentation during barrier formation.

The modeled distributions from hydrolyzed 5-week suberin showed a significant contrast between C16 and C24. C16 chains exhibited a broad distribution of isotopologue patterns reflecting the incorporation of singly and doubly labeled acetyl groups, whereas C24 chains additionally included a sharper increase in m/z by 2 for the initial *de novo* chains (i.e., chains with ^{13}C only) from elongation, M+2 to M+8 (Fig. 6a,b). Across the developmental series, this framework revealed a shift in carbon allocation rather than a general increase in lipid synthesis. Newly synthesized C16 in extractable lipids fell from 3 to 4 weeks, whereas newly synthesized suberin increased, with the strongest gain in C24 monomers (Fig. 6c,d). Thus, the onset of barrier formation coincides with redirection of carbon from bulk membrane/extractable lipids toward VLC suberin assembly, consistent with the VLCFA-rich barrier chemistry defined in Fig. 2. This compartmentation matches current models of plant lipid metabolism, in which plastids produce C16/C18 acyl chains and the ER elongase complex converts them into VLCFAs [59,60].

We next asked how this flux architecture responds to low oxygen. Five-week plants were grown for one week under either control conditions or 1% O_2 with elevated CO_2, while continuously supplied with [U-^{13}C]glucose (Fig. 6e). Despite the visibly robust growth under hypoxia, ISA indicated that synthesis of both extractable lipids and suberin monomers declined, and that the decrease affected both C16 and C24 pools (Fig. 6f,g). In other words, low oxygen suppressed both plastidial fatty-acid synthesis and ER elongation. This result partly agrees with broader hypoxia literature, which shows that oxygen deprivation constrains membrane-lipid synthesis and drives extensive lipid remodeling [61,62]. It differs, however, from the canonical rice paradigm.

In rice, waterlogging and reduced-soil cues promote an outer-root barrier to radial oxygen loss by increasing exodermal suberization and lignification, thereby conserving oxygen for the apex [17,18,63]. Recent work further shows that low nitrate under waterlogging is a strong trigger for this response [18], emphasizing that rice barrier induction depends on the chemistry of the reduced rhizosphere as well as on oxygen status. The functional outcome in rice is clear, where basal oxygen leakage is restricted by a tighter outer barrier. *Typha* operates under a different physiological regime. Its roots already possess high porosity, strong internal aeration and substantial subapical oxygen release without the ADH and ethanol accumulation expected from internal oxygen failure [15,16]. Under this regime, retaining oxygen may be less limiting than maintaining a controlled soil interface while preserving internal transport.

Fluorol Yellow staining clarified how that balance is achieved. Under control conditions, both exodermal and endodermal suberin were visible, whereas under hypoxia the exodermal barrier was retained but endodermal signal was strongly reduced except in a few pole-associated cells (Fig. 6h). The hypoxic response in *Typha* is therefore not a global barrier induction, but selective remodeling. The exodermis—the outer, soil-facing barrier most relevant to radial oxygen loss and apoplastic exclusion—is preserved, whereas the endodermis, which regulates exchange with the stele, remains more plastic [20,64]. This interpretation is consistent with growing evidence that endodermal suberin is a dynamic barrier that can be both assembled and degraded, and that unsuberized passage cells preserve vascular access across an otherwise sealed cylinder [65,66].

The acetyl-CoA estimates point to the same conclusion. Under hypoxia, the relative contribution of glucose derived lipogenic acetyl-CoA increased in two plastid-associated pools even as absolute lipid synthesis fell (Fig. 6i), suggesting reduced dilution of a smaller active precursor pool rather than enhanced fatty-acid production. The data therefore argue against a simple model in which *Typha* uses fatty-acid synthesis as a major sink for excess reductant during oxygen limitation. Furthermore, the observed increase in M+2 acetyl-CoA labeling, as a proportion of the labeled pool, indicates altered glucose catabolism under hypoxia (Supplemental Fig. S6). This shift may support a reduction in the mixing of unlabeled carbon and the intermediates of metabolized ^{13}C glucose in the roots, hinting at alterations in oxidative pentose phosphate pathway (OPPP) and other pathways. Consistent with this view, lipid-MFA, recently developed for complex lipid networks [67], showed broad reductions in flux through plastidial desaturation and downstream glycerolipid assembly (Fig. 6j,k, Supplemental table S21, S22), reinforcing the
conclusion that low oxygen in *Typha* does not drive compensatory lipogenesis, but instead coincides with a general contraction of membrane lipid production while the outer root barrier remains intact.

These differences identify *Typha* as a useful model for unresolved questions that rice does not fully address. We still need to understand what signals preserve exodermal suberin while relaxing the endodermis, whether the two plastidial acetyl-CoA pools correspond to distinct cell types or metabolic states, and how oxygen, CO_2 and carbon reserves are balanced to sustain growth in flooded anoxic soils. Because *Typha* combines continued growth, selective barrier remodeling and flexible carbon allocation

under hypoxia, it provides a tractable system for dissecting how wetland plants maintain productivity where many crops fail [68].

Conclusions

The results reported here position *T. domingensis* as a mechanistically tractable wetland plant. We show that marsh adaptation in *Typha* emerges from the coordination of clonal integration, pressurized internal aeration, chemically specialized suberin barriers and flexible carbon allocation to root surface protection. The Typha root is not simply more suberized than crop roots; it builds a distinctive VLCFA, hydroxycinnamate-rich barrier, and supports it through shoot-derived sucrose, serine-linked one-carbon metabolism and selective redistribution of lipid flux. Under hypoxia, *Typha* further reveals that resilience does not require generalized barrier induction: instead, it preserves the exodermal interface while remodeling inner barriers and contracting bulk lipid synthesis. These features help explain why *Typha* remains productive in flooded marshes and underscore the value of wetland plants as reservoirs of adaptive design principles. *Typha* species as a reference plants should therefore inform the functioning of wetland ecosystems and the engineering of crop plants to maintain growth, root function and carbon economy under increasingly unstable climates.

Methods

Plant Material:

Southern cattail (*Typha domingensis*) used for chemical analyses was collected from a stand in the Batiquitos Lagoon, in Carlsbad, CA in the summer of 2022. Soybean (*Glycine max* 'S99-2881'), Rice (*Oryza sativa* 'T422-57') and Wheat (*Triticum aestivum* 'Cltr 14108') used in this study were grown in spring/summer of 2022 in 20-liter pots filled with Turface® MVP™ calcined clay (Turface Athletics, Buffalo Grove, IL) at the Salk Institute Greenhouse Facility at Leichtag Commons, in Encinitas, CA. While rice pots were subjected to a 20-day flooding treatment at 40 days after planting (DAP), with the pots continually saturated, followed by a 10 day drying, soybean and wheat were grown aerobically for all 70 days. Root material from these 70 day old plants, as well as *Typha* collected in the wild, were cleaned, dried for 72 hours at 50 °C, then milled with a Retsch Ultra Centrifugal Mill ZM 200 (Verder Scientific, Inc., Newtown, PA).

Adult *Typha* used for Scanning- and Transmission- Electron Microscopy and floural yellow staining of suberin, were collected across from the UCSD campus. *Typha* plants used for genome sequencing were collected in San Diego, CA, State College, PA and across selected regions of coastal Louisiana. In Louisiana, plants largely come from the Birdsfoot region of the Mississippi River Delta, and the Lake Pontchartrain Basin, which are freshwater or low salinity environments (Supplemental table S6). When possible, California plants were collected from CalFora locations (Calflora.org). Whole plants, including

their roots, were removed from sampling locations by hand, using a small shovel. Sampling latitude and longitude were recorded using either a hand-held GPS or a smart phone. Whole plants from Louisiana were placed wet in plastic bags and shipped within 1-3 days of collection to the Salk Institute via an express shipper. Plants were potted and grown under growth room conditions at the Salk Institute. Leaf cuttings were taken from new leaf growth and immediately frozen in liquid nitrogen for DNA extraction.

Seedling growth for *Typha domingensis* developmental and ^{13}C labeling studies

Seeds collected from wild *Typha domingensis* plants often yielded less than 30% germination rates.To improve fertility, wild collected plants were potted, grown to maturity and hand pollinated. These seeds were surface sterilized with 70% ethanol and 30% bleach followed by repeated washing with sterile water. Seeds were incubated in the dark at 4 °C for 4 days before planting on 10 x 10 cm square plates containing ½ MS nutrient media supplemented with 1% glucose solution. Plates were grown vertically in a growth chamber with 16-hour light and 8-hour dark cycles. For transcriptomic studies and microscopy, roots and shoots of the seedlings were collected separately at 3, 4 and 5 weeks after planting (WAP).

For $^{13}CO_2$ labeling experiment, individual seedlings at the end of 5 WAP were transferred to 5 mL vials filled with ½ MS nutrient solution without nitrogen, supplemented with 5 mM $^{15}NH_4{}^{15}NO_3$ but no carbon source. Vials were incubated in a custom-built labeling chamber (Fig 5a) hooked to a custom gas mixture containing air mixture at 425 PPM $^{13}CO_2$, 21.9% oxygen and balanced with nitrogen. Isotopically enriched $^{13}CO_2$ was estimated to be at 99% purity. Labelled gas mixture was continuously supplied to the chamber at 1 mL/min for the 24 hours of labeling experiment. Four replicate vials were removed from the chamber at the appropriate time points, roots and shoots separated, flash frozen and stored at -80 °C until further analysis.

For [U-^{13}C]glucose tracing experiments, seedlings were grown in plates containing ½ MS media supplemented with glucose for 2, 3 and 4 weeks and transferred to new plates that contained ½ MS supplemented with [U-13C]glucose to continue growth for an additional week to obtain 2, 4 and 5 WAP plants for analysis. For hypoxia treatment, 4-week-old seedlings were transferred similarly transferred to [U-13C]glucose containing media and grown for one week vertically in a hypoxia chamber (Coy laboratory products, Michigan, USA) that was fed a custom mixture of 2% O_2, 0.1% CO_2 and balanced with N_2. A stagnation experiment was used as a control for hypoxia, where 4 week old plants were transferred to an oxygen scrubbed ½ MS medium supplemented with [U-13C]glucose, following protocol described by de la Cruz Jimenez et al. (2021) [69], and incubated for one week. At the end of all experiments seedlings were removed, quickly rinsed with deionized water, flash frozen upon separation of roots and shoots and stored at -80 °C until further analysis.

Solid-state NMR:

16 mg of dried ground root samples from plant collection described above were packed into a 3.2 mm Phoenix MAS 22 µL zirconia rotor. Solid-state NMR measurements were carried out at UC Merced in a 89

mm 11.7 T (499.72 MHz) Agilent NMR system equipped with Agilent DD2 console equipped for high-power solid-state NMR using an Agilent T3 3.2 mm probe. The sample spinning rate was 10 kHz and sample temperatures were regulated at 25 ^{o}C, including a correction for frictional heating. We carried out ^{1}H-^{13}C Cross-Polarization (CP-MAS) and ^{13}C Direct Polarization (DP-MAS) detected experiments. Field strengths for ^{13}C cross-polarization were all 50 kHz with a 10% ^{1}H linear ramp centered at 57 kHz. CP-MAS was followed by echo acquisition using a 10 us Pi refocusing pulse. For CP-MAS mixing time was 1 ms, recycle delay was 3.0 s with 8k scans, for DP recycle delay was 20 s with 10k scans. The chemical shift frequencies were referenced externally to the adamantane methylene ^{13}C resonance at 38.5 ppm [70]. All data was processed on Bruker Topspin, apodized with 30 Hz (CP-MAS) or 100 Hz (DP-MAS) exponential line broadening before zero-filling, followed by Fourier transformation. Integration errors were estimated experimentally by measuring the sign-to-noise ratio for each spectral region. Figures were annotated and edited with Adobe Illustrator.

Floural Yellow staining for suberin

Live roots of *T. domingensis* collected 3-week, 4-week, 5-week old sterile media grown plants, and mature plants collected from the wild, were manually cut in 3-mm fragments with a razor blade at the older region of root. These fragments were fixed in a solution containing 4% paraformaldehyde (EMS) in 0.1 M phosphate buffer saline (EMS) under microwaves (Pelco BioWave Pro) for 2 min at 45^{o}C and kept for an additional 1h at RT. Samples were then rinsed 5 x 10 min in PBS, quenched for 20 min in 50 mM glycine in PBS, tissue cleared in ClearSee solution for 5 days, incubated in fluorol yellow (FW) 088 (BOC Sciences) (0.01% w/v, dissolved in lactic acid) for 2 h at RT protected against light, rinsed 5 x 10 min each with DI water and finally mounted with Prolong Gold (Invitrogen) on glass slides / coverslips. Samples were imaged on a confocal microscope Zeiss LSM 880 Airyscan using 20X and 63X (NA 1.4) objectives, 488 nm excitation, 500-550 nm emission.

Transmission (TEM) and Scanning Electron Microscopy (SEM)

Same plants as described above were fixed in a solution of 4% paraformaldehyde (EMS), 2.5% glutaraldehyde (EMS), in 0.1M sodium cacodylate buffer (EMS) under microwaves (Pelco BioWave Pro) for 2 min at 45^{o}C and kept for an additional 1 h at RT. Samples were washed in the same buffer 3 x 15 min, post-fixed with aqueous 1.5% osmium tetroxide (EMS) for 1 h, washed for 3 x 15 min, stained with aqueous 1% uranyl acetate for 30 min, washed for 3 x 15 min, dehydrated in graded ethanol series until absolute (3x) 15 min each time. For SEM, samples were critical-point-dried (Leica EM CPD300), mounted using carbon tape on aluminum stubs, gold-sputtered (Leica EM SCD500) for 2 min, and observed on a Zeiss Sigma VP, operating at 5 kV. For TEM, the dehydrated samples were embedded in Spurr resin (EMS), sectioned on a ultramicrotome (Leica UC7) at 60nm-thickness, stained with UranyLess (EMS) for 5 min, and observed on Zeiss Libra 120, operated at 80 kV.

Soxhlet extraction and depolymerization of extractable lipids and suberin residue

A Soxhlet extraction with solvents of increasing polarity (dichloromethane, ethanol, and water) was used to separate extractible lipids from dried ground root material. The root residue after the soxhlet extraction was air-dry and kept for the second step, following the method described in Pereira H (1988) [71]. All phases from the filtration (insoluble, precipitation residue, and the supernatant) were analyzed for fatty acid monomers following depolymerization and derivatization using gas chromatography mass spectrometry (GCMS) following the method described in Molina et al., (2006) [72]. Briefly, 50 mg of solvent-extracted and dried residue (for suberin monomers) as well as pooled and dried extracts (for extractible lipid monomers) were incubated at 60°C for 2h in 6 ml of MeOH containing 15% (v/v) methyl acetate and 6% (w/v) NaOMe, with periodic vortexing. A deuterated (D_{31}) standard of Methyl hexadecanoate (Sigma, USA) was added as an internal standards at 1 mg/g dry residue each. The reaction mixtures were acidified with glacial acetic acid to pH 4–5, saline added and the fatty acid methyl esters (FAMEs) extracted with CH_2Cl_2 (10 ml). The organic phase was washed three times with dilute saline solution (0.5 M NaCl) and dried under a gentle stream of N2. The resultant product was additionally silylated to convert hydroxyl groups to their TMSi ethers for quantification using Gas Chromatography- Mass Spectrometry (GC-MS). Derivatized samples were dried under nitrogen, resuspended in 1:1 toluene: heptane mixture and transferred to glass vials for analyses.

GC-MS of FAMEs and TMSi ethers of fatty acids

GC MS analysis was carried out using a HP5-MS ultra inert capillary column (J & W scientific, CA, USA) that is 30 m x 0.25 mm x 0.25 µm hooked to an Agilent 7890B GC and 5977B MS system equipped with a Gerstel multipurpose sampler. 1 µL of sample was injected into an inlet maintained at 300 °C, operating in splitless mode with Helium as the carrier gas at 1 mL/min constant flow. Oven temperature was programmed to hold initially at 60 °C for 2 min followed by a 6 °C/min ramp to 320 °C where it was held for 5 min. The MS was operated in scan mode over 50-700 amu with electron impact ionization at a frequency of 4.4 scans/sec and ion source temperature maintained at 200 °C. Data were integrated using chemstation software and accurate quantities were determined using an external standard curve for all measured monomers using authentic standards relative to hexadecanoic (C17:0) for FAMEs, 17-hydroxy hexadecenoic (C17:0, ωOH) for 1°-Alcohols and ωOH fatty acids, and hexadecanedioic acid (C17:0, diacid), for diacids, spiked in as internal standards at known concentrations.

TMAH/Thermochemolysis GC-MS

Sterile plate grown samples with low root biomass were measured for extractable lipid and suberin fatty acid monomers using thermochemolysis followed by GC-MS as described previously [73]. 20-30 mg of fresh root tissue was collected and extracted for soluble lipids following method previously described [72]. All solvent fractions used for extraction were pooled and dried under nitrogen. The remaining residue that contains suberin was also dried and both fractions were analyzed on a Shimadzu QP2020-NX GCMS equipped with a Frontier multishot EGA PY3030D pyrolyzer. 5 µL of tetramethyl ammonium hydroxide (TMAH) and 1 µg of (Z)-10-pentadecanoic acid methyl ester (C15:1) internal standard were added to dried samples and heated at 350 °C with an inlet temperature of 300 °C and split flow of 20:1. Volatized

compounds were separated on a SH-Rxi-5ms column (Shimadzu, 30 m, 0.25mm id) at a column flow of 1 mL/min from 60 °C to 320 °C with temperature ramp of 6 °C/min then held at 320 °C for 5 min. Mass data was collected from m/z 50-700 with ion source temperature of 200 °C. C16, C18 and C24 FAME concentrations were calculated by extracted ion external calibration curves with FAME standard mix (Matreya LLC) relative to the internal standard using unlabeled samples. For U-13C glucose enriched samples, used for isotope spectral analysis (ISA), raw data files were first convered to mzML format using MS Convert within proteowizard, and FAME peaks along with their isotopologues were integrated using El-Maven. Exported peak areas were corrected for natural abundance using IsoCorrectoR and ISA was performed using INCA.

Genome size estimates

Nuclear DNA size estimates of *Typha domingensis* and *Typha latifolia* were determined by flow cytometry from the method described in Arumuganathan and Earle (1991) [74].

DNA extraction

DNA was extracted from frozen tissue per previous methods with modifications [75]. High molecular weight (HMW) DNA was extracted from leaf tissue of *Typha* plants using a modified bomb protocol (https://bomb.bio/protocols/). Resulting DNA was quality controlled using Qubit for quantitation and gel electrophoresis to confirm the presence of high molecular weight (HMW) DNA. Samples with sufficient concentration and of HMW were used for sequencing.

Genome Sequencing

Unsheared HMW DNA was used to make Oxford Nanopore Technologies (ONT) ligation-based libraries. Libraries were prepared starting with 1.5 ug of DNA and following all other steps in ONT's SQK-LSK109 protocol. Final libraries were loaded on an ONT flowcell (v9.4.1) and run on the GridION. Bases were called in real-time on the GridION using the flip-flop version of Guppy (v3.1). The resulting fastq files were concatenated and used for downstream genome assembly steps. One flowcell per *Typha* genome generally produced enough data for complete assemblies. Illumina 2x150 paired-end reads were also generated for genome size estimates and polishing genome sequences. Libraries were prepared from HMW DNA using NEBNext (NEB, Beverly, MA) and sequenced on the Illumina NovaSeq. The resulting raw sequence was only trimmed for adaptors, resulting in >60x coverage of the *Typha* genome.

RNA Sequencing

Root and Shoot samples for RNA sequencing were collected from 3-5 week sterile plate grown plants. RNA was extracted using protocols for the RNeasy Plant Mini Kit. Total RNA was quantified with a Nanodrop and appropriate dilutions were made for Oxford Nanopore's SQK-PCS109 full-length PCR cDNA sequencing kit. Each sample was uniquely barcoded and pooled for sequencing on a single GridION flowcell. Libraries were sequenced twice and reads for the technical duplicates concatenated

prior to mapping. Reads were mapped to the TD08 coding sequences with Minimap2 (v 2.17-r941) [76] and quantified using Salmon (v1.10.3) [77]. Differential expression was performed with edgeR (v3.36.0) using pairwise comparisons [78]. Homologous genes from Arabidopsis thaliana were assigned by blasting [79] the TD08 proteome against the Arabidopsis TAIR10 proteome using an e-value cutoff of <0.01. and the top hit retained.

HiC library preparation

Crosslinking was performed on ground tissue and nuclei were isolated following https://www.protocols.io/view/*Typha*-cattail-crosslinking-and-nuclei-isolation-bf5gjq3w. HiC data was generated using the Arima-HiC Kit User Guide for Plant Tissues [80], according to the manufacturer's protocols (A510008 D. Libraries were generated following the Arima-HiC Kit Library Preparation Guide for Swift Biosciences Accel-NGS 2S Plus DNA Library Kit (CA510008).

Genome assembly

The resulting fastq files passing QC (fastq_pass) were assembled using our previously described pipeline [81]. Briefly, fastq files were filtered by length for the longest 30x using an Illumina kmer-based genome size estimate. The 30x fastq files were overlapped using minimap2 [76], the initial assembly was generated with miniasm [82], the resulting graph (gfa) was visually checked with Bandage [83], the assembly fasta was extracted from the gfa **(awk '/^S/{print ">"$2"\n"$3}'** assembly_graph.gfa | fold >assembly_graph.fasta), the consensus was generated with three iterative cycles of mapping the 30x reads back to the assembly with minimap2 followed by Racon[84], and the final assembly was polished iteratively 3 times with using 2x150 bp paired-end Illumina reads mapped using minimap2 (>98% mapping) followed by pilon[85].

HiC scaffolding

The polished TD08 and TL01 assemblies were scaffolded using reads from their respective HiC libraries. We used standard methods defined in the Aiden lab genome assembly cookbook [86]. The primary steps include alignment of HiC reads to the draft assembly and creation of a contact map using the Juicer pipeline v1.6.2) followed by automated scaffolding using 3d-dna v180419) both executed with default options. The scaffolds were then inspected and manually corrected with Juicebox Assembly Tools JBAT) v1.11.08. The resultant scaffolds for TD08 and TL01 were then aligned to each other using minimap2 to label chromosomes with consistent synteny.

Genome quality

The final assemblies were checked for completeness using BUSCO: Benchmarking Universal Single-Copy Orthologs [87]. In general the BUSCO scores were very high (>95%) and were consistent with homozygous genomes due to the low number of "Complete and duplicated BUSCOs IDs". The genomes

then were assessed for repeat content using tandem repeat finder (TRF) [88]. The TRF output was transformed and searched for simple repeats, telomere repeats (AAACCCT), and putative centromeres as previously described [89]. The genomes did not contain an unusual level of simple and short repeats. All the genomes contained exceptionally long telomere sequences (average between 10-20 kb). Utilizing the telomere sequence the full-length chromosomes were identified and ranged from 1 to 6 in the *Typha* genomes. Unlike most plant genomes, *Typha* does not have an overrepresented centromere repeat. We also searched the genomes for mitochondria (MT), chloroplast (CP) and ribosomal DNA (rDNA) 25s and 5s sequences. Most assemblies had either a full-length MT or it was found in two pieces. In contrast, all assemblies had multiple versions of the CP genome ranging in size from 70 kb (missing the inverted repeat) to >400 kb (including several CP copies). Almost all of the assemblies contained a single 25s rDNA array consistent with one array on chromosome X.

Genome annotation

All genomes were annotated using a pipeline consisting of four major steps: repeat masking, transcript assembly, gene model prediction, and functional annotation. Repeats were identified using EDTA [90] and these repeats were used for softmasking. ONT cDNA reads were aligned to the genomes using minimap2 and assembled into transcript models using Stringtie. Softmasked genomes and Stringtie models were then processed by Funannotate (v1.6) (https://github.com/nextgenusfs/funannotate) to produce gene models. Predicted proteins were then functionally annotated using Eggnog-mapper (v2) [91]. For the non-reference genomes proteins were predicted with funannotate.

PanKmer analysis

PanKmers indexing uses de novo assembled genomes and counts unique canonical Kmers of size 31, and assigns each Kmer a binary value that indicates which samples have that canonical Kmer [92]. Reverse complement kmers are excluded. A dictionary of kmers is generated where the keys are Kmers and the values are numbers (bits). Each bit score harbors the information about presence absence in each genome sample, thus creating a list of kmers without the need of a reference. The rolling average percent identity is calculated for each sample relative to a chosen genome for visualization.

Orthogroup analysis and synteny

Comparative genomic analyses were performed across 24 angiosperm proteomes (939,635 proteins total) using OrthoFinder v3.1.5 [93,94] with DIAMOND v2.2.4 [95] for all-versus-all BLAST searches and the inferred rooted species tree (rooted at *Amborella trichopoda*). OrthoFinder clustered all proteins into 110,446 orthogroups, of which 29,539 contained two or more genes. Gene family evolution was modeled with CAFE5 v5.1.0 [96] on the 7,915 families present at the root after strict filtering (removing families with >50 genes in any species), estimating a single birth–death lambda parameter ($\lambda = 1.35$) and identifying families with significant expansion or contraction at $p < 0.05$. Orthogroup copy-number differences between each *Typha* species (*T. latifolia*, *T. domingensis*) and three Oryza species (*O. rhizomatis*, *O.*

glaberrima, *O. nivara*), both individually and as a grouped set, were assessed with OrthoPos comp v0.2.0 [97] using Fisher's exact test with Benjamini–Hochberg FDR correction (FDR < 0.05). GO enrichment of orthogroups was performed with OrthoPos gos v0.2.0, using GO annotations from five proxy species (*Arabidopsis thaliana*, *Glycine max*, *Oryza glaberrima*, *Oryza nivara*, and *Triticum aestivum*) downloaded from UniProt [98], with the GO ontology (go-basic.obo) used to propagate scores from child to parent terms. All analyses were performed on a single set of orthogroup IDs from the OrthoFinder v3.1.5 run, ensuring full cross-referencing between CAFE5, OrthoPos comp, and OrthoPos gos results.

Starch Quantification

Starch hydrolysis was performed using 50 mg of fresh tissue, upon extraction of free glucose with hot 80% ethanol, in triplicates, using the Megazyme starch assay kit (Megazyme International Ireland), using the AOAC Official Method 996.11 (Approved Methods of AOAC [99]). Hydrolyzed glucose was measured using GC-MS upon derivatization as aldonitrile pentapriopionate following the method previously described by Antoniewicz et al. (2011) [100], with no modifications. Peak area for the fragment with m/z 370 was integrated and accurate quantities determined by comparing to a standard curve derived from a starch serial dilution which was hydrolyzed and the resultant glucose derivatized and measured alongside the samples.

Total metabolite extraction

Approximately 100 mg of fresh tissue was homogenized using a tissue lyser, and extraction was carried out using a phase separation method previously described [51]. Briefly, 1 mL of chilled 7:3 methanol: chloroform containing a mixture of small molecule (Norvaline, Ribitol, 1,4-piperazinediethanesulfonic acid) and deuterated lipid (UltimateSPLASH^{TM} One, Avanti Polar Lipids) internal standards at known concentrations. Samples were sonicated for 10 minutes, vortexed thoroughly and incubated on a rotary shaker for 4h at 4 °C. After incubation, 500 µL of ice-cold water was added to the samples, vortexed and centrifuges at 14,000 rpm at 4 °C for 10 min to achieve phase separation. The upper aqueous phase was carefully transferred to a new tube. 200 µL of methanol added to the remaining organic phase containing lipids and centrifuged at 14,000 rpm for 5 min to pellet the debris and supernatant was transferred to a new tube. Both acqueous and the organic phases were dried using a speedvac centrifuge. Acqueous phase samples were resuspended in 100 µL of 50% methanol and used for metabolomics while the organic phase samples were resuspended in 100 µL of 49:49:2 acetonitrile: methanol: chloroform for lipidomics analyses.

Metabolomics and Lipidomics measurements

Two chromatographic methods, one using a hydrophilic interaction (HILIC) and the other using a reverse phase (RPLC) were performed for metabolomics to ensure detection of a wide diversity of compound classes. HILIC separation was achieved using an Agilent InfinityLab Poroshell 120 HILIC-Z (2.1 x 100 mm x 2.7 µm) column using 20 mM ammonium carbonate and 5 µM medonic acid, in water as solvent A

and in 95:5 acetonitrile: water as solvent B. 3 µL of sample was injected and compounds were separated using 0.3 mL min^{-1} flow rate following a gradient elution that decreases from 100% B to 90% B over 4 mins, then to 50% B over the next 6 minutes. Gradient was reduced to 30% B over the next 0.5 mins and held there for 1 min after which it was brought back to 100% B and equilibrated for 8 minutes before injecting the next sample. RPLC separation was achieved using an Acquity™ Premier HSS T3 1.8 µm VanGuard™ FIT (2.1 x 100 mm) column using water and acetonitrile both with 0.1% formic acid as solvents A and B respectively. 5 µL of sample was injected and compounds were separated using 0.25 mL min-1 flow rate following a gradient elution that increased from 5% B to 95% B over 11 minutes, followed by a 1 min hold and then decreased to 5%. The column was equillibrated for 7 minutes before injecting the next sample.

Lipidomics measurements were performed using a Nucleodur C8 Gravity (2.1 x 100 mm x 5 µm) column (Machery-Nagel, Allentown, PA) following a method previously described [101]. Briefly, 5 µL of sample was injected and compounds were separated using 0.25 mL min-1 flow rate with a gradient elution achieved by 1M ammonium acetate and 0.1 % acetic acid in water (solvent A) and 1M ammonium acetate and 0.1% acetic acid in 7:3 acetonitrile: IPA (solvent B). The following gradient conditions were used: 0-1 min at 55% B, 4 mins at 75% B, 12 min at 89% B, 15 min at 99% B, 18 min at 99% B; 18.5 min at 55% B and equilibration at 55% up to 24 min.

The eluent for all three methods was sprayed onto a HESI II source of a qExactive Orbitrap mass spectrometer, operated with sheath gas, 25 arbitrary units; auxiliary gas, 5 arbitrary units; ion transfer tube temperature, 300 °C; vaporizer temperature, 100 °C; and S-lens RF level, 60. The spray voltage was 3.5 kV in positive mode and 3 kV for negative mode. Metabolomics methods were operated in a polarity switching mode with Full MS data collected for mass ranges 70-800 m/z at 70,000 resolution. Lipidomics data were collected for mass ranges 450–1200 *m/z* at 140,000 resolution with both positive and negative mode acquisition using separate injections. MS/MS data were collected for representative pooled unlabeled samples using a data dependent acquisition.

Peak areas were integrated using El-Maven[102]. Data were exported as comma delimited files and used as appropriate for downstream analyses. For small molecules, isotope enrichment data were rearranged in a format required by SIMPEL[51] and analyzed following the tutorial, along with a database of compounds. Compounds were identified using authentic standards were available and/or comparison to literature and library spectra. For small molecules, accurate quantities were calculated using external standard curves upon normalization to an internal standard. Where standards are unavailable, a structurally similar compound was used for quantification. Lipid quantities were calculated by comparing each lipid species to their closest standard, by chain length, from within the UltimateSPLASH ONE mix that was spiked into the samples. While natural abundance correction for small molecules was performed within SIMPEL, lipid labeling used for metabolic flux analyses, was first corrected using IsoCorrectoR [103] and corrected data were used for downstream analyses.

^{13}C Lipid Metabolic Flux Analysis

ISA and MFA were performed to estimate the percent of newly synthesized lipids as well as the contribution of the tracer of interest to lipogenic acetyl-CoA pools, glycerol-3P turnover and metabolic flux necessary to maintain the measured lipid pools. While measured lipid pools were fixed to the absolute abundances calculated and presented in the manuscript, no constraints were set for the acetyl-CoA or glycerol-3P used by the network. Initially, one plastidial acetyl-CoA pool was used to perform ISA on fatty acid synthesis, however, a one pool network could not generate the high D value, and lower D value signatures that were deconvoluted though ISA. χ^2 statistical test was applied to assess the goodness-of-fit using α of 0.01. Parameters for contribution of ^{13}C tracers to lipogenic acetyl-CoA (*D* value) and percentage of newly synthesized lipids [*g*(*t*) value] and their 99% confidence intervals are then calculated using best-fit model after estimating 100 times using random initial guesses for all fluxes in the network in INCA MFA (isotopomer network compartmental analysis metabolic flux analysis) software [104].

Experimental lipid labeling from [U-$^{13}C_6$] glucose after a 7-day trace was compared to simulated labeling using the ISA and Lipid-MFA reaction networks provided with the manuscript and found in Supplemental tables S17 and S21, respectively. Experimental replicates were averaged to generate mean mass isotopomer values for each lipid. Estimated flux values and parameter continuation were performed using the mean value and a standard deviation for the representative mass isotopomers. Mass Isotopomer distributions were entered into INCA after natural isotope correction using IsoCorrectoR[103] . When background noise in the mass isotopomer distributions were identified from ^{12}C labeling wells or in regions with unexpected labeling, that mass isotopomer value was replaced with “NaN” to ignore the value during flux estimation and parameter continuation. This resulted in less than 5% of all mass isotopomers being removed. This was necessary due to coelution of lipid species with similar masses and the added isotopic complexity resulting from the addition of stable isotope tracing.

MFA data are plotted as 95% confidence intervals. “*” indicates statistical significance by non-overlapping confidence intervals. Calculated fluxes, pool size data used for sinks, and isotopologue data used within INCA can be found in Supplemental tables S18, S19, S20 for ISA and S22, S23 and S24 for lipid-MFA.

^{13}C metabolic flux analysis was conducted under the following assumptions:

1. Roots were assumed to be at metabolic and isotopic steady state.
2. Growth and accumulation of lipids in the root were modeled with a homogenous metabolism over the course of 7 days of growth with the measured lipids representing the results of both light and dark cycles.
3. Two plastidial Acetyl-CoA pools were used to model the synthesis of fatty acids due to the underlying and overlapping labeling distributions observed in the MIDs.

Declarations

Reporting summary

Further information on research design is available in the Nature Portfolio Reporting Summary linked to this article.

Data availability

All data are publicly available through the National Center for Biotechnology Information (NCBI). The chromosome-scale genome assemblies and annotations reported in this study have been deposited in GenBank under accession numbers GCA_019914945.2 (*Typha latifolia*) and GCA_056512515.1 (*Typha domingensis*) within BioProject PRJNA622838. Raw Oxford Nanopore Technologies (ONT) and Illumina sequencing data have been deposited in the NCBI Sequence Read Archive (SRA) under BioProject PRJNA742003. Raw, pre-processed and annotated data for metabolomics and lipidomics dataset for *Typha d.* developmental studies is available at NIH Common Fund's National Metabolomics Data Repository (NMDR) webside, the Metabolomics Workbench, https://www.metabolomicsworkbench.org/ , under project number XXX (DOI:XXX). Raw and annotated data for stable isotope tracing with $^{13}CO_2$ and [U-^{13}C]glucose is also available within the same project under study ID XXX.

Author Contributions

S.K., J.P.N. conceived and designed the experiments, S.K., L.A., B.W.A., K.W.R., A.D., S.T.T., J.P., J.J.L., C.P., R.N.R., J.Z., N.A., N.T.H., N.A., N.T.H., D.H.M., performed research, programming and data analysis, D.K.A., T.P.M., C.M.M, J.P.N contributed to the experimental design, result interpretation and funding acquisition, S.K. wrote the initial manuscript and all authors contributed to editing and reviewing.

Competing interests

T.P.M. and J.P.N. are co-founders of Cquesta, Inc., a company that works on crop root growth and carbon sequestration. All other authors declare no competing interests.

Acknowledgments

The plant collection, propagation and genome work were funded by the following awards to Joseph P. Noel, the Howard Hughes Medical Institute, the Salk Institute Arthur and Julie Woodrow Chair, the Chambers Medical Foundation, the Kitzmiller-Moran Challenge Funds, and the Joe W. and Dorothy Dorsett Brown Foundation. This work was also supported by donations from Howard and Maryam Newman and The Howard and Maryam Newman Family Foundation, gifts to the Salk Institute's Harnessing Plants Initiative (HPI) from the Bezos Earth Fund, the Hess Corporation, and through the TED Audacious Project. We thank Dr. Anna Heller, Dr. Vladimir Maslivetc, Dr. Xuelin Wu, Dr. Lauren Whitt and Dr. Alex Harkess for their input during conversations about *Typha* work. We thank Dr. David Rice from UC Merced for NMR experiments. We also thank a series of earlier conversations with Melissa Baustain, Leeland Moss, Christopher Esposito, Emily Farrer, Kathleen Ferris, Theryn K. Henkel, Eva Hillman, and Alexander S. Kolker for stimulating discussions and identification of Louisiana Typha populations that

contributed to the early conception of this project. ChatGPT 5.0 was used for language editing in the main manuscript.

References

1. Rogers, K. *et al.* Wetland carbon storage controlled by millennial-scale variation in relative sea-level rise. *Nature 2019 567:7746* **567**, 91–95 (2019).
2. Crooks, S. *et al.* Coastal wetland management as a contribution to the US National Greenhouse Gas Inventory. *Nature Climate Change 2018 8:12* **8**, 1109–1112 (2018).
3. Bailey-Serres, J. & Voesenek, L. A. C. J. Flooding stress: acclimations and genetic diversity. *Annu. Rev. Plant Biol.* **59**, 313–339 (2008).
4. Bansal, S. *et al.* Typha (Cattail) Invasion in North American Wetlands: Biology, Regional Problems, Impacts, Ecosystem Services, and Management. *Wetlands 2019 39:4* **39**, 645–684 (2019).
5. Grace, J. B. Effects of water depth on Typha latifolia and Typha domingensis. *Am. J. Bot.* **76**, 762–768 (1989).
6. Mufarrege, M. M., Di Luca, G. A., Hadad, H. R. & Maine, M. A. Adaptability of Typha domingensis to high pH and salinity. *Ecotoxicology 2011 20:2* **20**, 457–465 (2011).
7. Gashu, K., Kaste, J. A. M., Roje, S. & Walker, B. J. Metabolic flux analysis in leaf metabolism quantifies the link between photorespiration and one carbon metabolism. *Nature Plants 2025 11:9* **11**, 1877–1889 (2025).
8. Mitsch, W. J. . & Gosselink, J. G. . *Wetlands*. (John Wiley & Sons, Inc., 2015).
9. Kirwan, M. L. & Mudd, S. M. Response of salt-marsh carbon accumulation to climate change. *Nature 2012 489:7417* **489**, 550–553 (2012).
10. Baustian, M. M. *et al.* Relationships Between Salinity and Short-Term Soil Carbon Accumulation Rates from Marsh Types Across a Landscape in the Mississippi River Delta. *Wetlands 2017 37:2* **37**, 313–324 (2017).
11. Shields, M. R. *et al.* Carbon storage in the Mississippi River delta enhanced by environmental engineering. *Nature Geoscience 2017 10:11* **10**, 846–851 (2017).
12. Kosma, D. K., Graça, J. & Molina, I. Update on the structure and regulated biosynthesis of the apoplastic polymers cutin and suberin. *Plant Physiol.* **197**, 653 (2025).
13. Bendix, M., Tornbjerg, T. & Brix, H. Internal gas transport in Typha latifolia L. and Typha angustifolia L. 1. Humidity-induced pressurization and convective throughflow. *Aquat. Bot.* **49**, 75–89 (1994).
14. Yin, Y. G. *et al.* Noninvasive imaging of hollow structures and gas movement revealed the gas partial-pressure-gradient-driven long-distance gas movement in the aerenchyma along the leaf blade to submerged organs in rice. *New Phytologist* **232**, 1974–1984 (2021).
15. Duarte, V. P., Pereira, M. P., Corrêa, F. F., de Castro, E. M. & Pereira, F. J. Aerenchyma, gas diffusion, and catalase activity in Typha domingensis: a complementary model for radial oxygen loss. *Protoplasma 2021 258:4* **258**, 765–777 (2021).

16. Chabbi, A., Mckee, K. L. & Mendelssohn, I. A. Fate of oxygen losses from Typha domingensis (Typhaceae) and Cladium jamaicense (Cyperaceae) and consequences for root metabolism. *Am. J. Bot.* **87**, 1081–1090 (2000).
17. Yamauchi, T., Colmer, T. D., Pedersen, O. & Nakazono, M. Regulation of Root Traits for Internal Aeration and Tolerance to Soil Waterlogging-Flooding Stress. *Plant Physiol.* **176**, 1118–1130 (2018).
18. Shiono, K., Ejiri, M., Sawazaki, Y., Egishi, Y. & Tsunoda, T. Low nitrate under waterlogging triggers exodermal suberization to form a barrier to radial oxygen loss in rice roots. *Plant Physiol.* **196**, 551–563 (2024).
19. Soukup, A., Armstrong, W., Schreiber, L., Franke, R. & Votrubová, O. Apoplastic barriers to radial oxygen loss and solute penetration: A chemical and functional comparison of the exodermis of two wetland species, Phragmites australis and Glyceria maxima. *New Phytologist* **173**, 264–278 (2007).
20. Enstone, D. E., Peterson, C. A. & Ma, F. Root Endodermis and Exodermis: Structure, Function, and Responses to the Environment. *Journal of Plant Growth Regulation 2003 21:4* **21**, 335–351 (2003).
21. Constable, J. V. H. & Longstreth, D. J. Aerenchyma Carbon Dioxide Can Be Assimilated in Typha latifolia L. Leaves. *Plant Physiol.* **106**, 1065–1072 (1994).
22. Constable, J. V. H., Grace, J. B. & Longstreth, D. J. High Carbon Dioxide Concentrations in Aerenchyma of Typha latifolia. *Am. J. Bot.* **79**, 415 (1992).
23. McNaughton, S. J. & Fullem, L. W. Photosynthesis and Photorespiration in Typha latifolia. *Plant Physiol.* **45**, 703–707 (1970).
24. Koley, S. *et al.* Metabolic synergy in Camelina reproductive tissues for seed development. *Sci. Adv.* **8**, 7683 (2022).
25. Schwender, J., Goffman, F., Ohlrogge, J. B. & Shachar-Hill, Y. Rubisco without the Calvin cycle improves the carbon efficiency of developing green seeds. *Nature* **432**, 779–782 (2004).
26. Gil, A. M., Lopes, M., Rocha, J. & Pascoal Neto, C. A 13C solid state nuclear magnetic resonance spectroscopic study of cork cell wall structure: the effect of suberin removal. *Int. J. Biol. Macromol.* **20**, 293–305 (1997).
27. Thomas, R. *et al.* Soybean Root Suberin: Anatomical Distribution, Chemical Composition, and Relationship to Partial Resistance to Phytophthora sojae. *Plant Physiol.* **144**, 299–311 (2007).
28. Schreiber, L., Franke, R., Hartmann, K. D., Ranathunge, K. & Steudle, E. The chemical composition of suberin in apoplastic barriers affects radial hydraulic conductivity differently in the roots of rice (Oryza sativa L. cv. IR64) and corn (Zea mays L. cv. Helix). *J. Exp. Bot.* **56**, 1427–1436 (2005).
29. Burger, D. J., Bauke, S. L., Schneider, F., Kappenberg, A. & Gocke, M. I. Root-derived carbon stocks in formerly deep-ploughed soils – A biomarker-based approach. *Org. Geochem.* **190**, 104756 (2024).
30. Barré, P. *et al.* Microbial and plant-derived compounds both contribute to persistent soil organic carbon in temperate soils. *Biogeochemistry 2018 140:1* **140**, 81–92 (2018).
31. Zosso, C. U., Ofiti, N. O. E., Torn, M. S., Wiesenberg, G. L. B. & Schmidt, M. W. I. Rapid loss of complex polymers and pyrogenic carbon in subsoils under whole-soil warming. *Nature Geoscience 2023 16:4*

16, 344–348 (2023).

32. Widanagama, S. D., Freeland, J. R., Xu, X. & Shafer, A. B. A. Genome assembly, annotation, and comparative analysis of the cattail Typha latifolia. *G3 Genes|Genomes|Genetics* **12**, (2022).
33. Li, Y. P. *et al.* The telomere-to-telomere genome of Pucai () (Typha angustifolia L.): a distinctive semiaquatic vegetable with lignin and chlorophyll as quality characteristics. *Hortic. Res.* **12**, (2025).
34. Du, J., Huang, L. & Xu, X. Chromosome-level genome assembly of the dwarf cattail Typha minima. *Scientific Data 2026 13:1* **13**, 231- (2026).
35. Aleman, A., Shafer, A. B. A., Freeland, J. R. & Dorken, M. E. Repeated cases of allopatric divergence and secondary contact in cattail (Typha) speciation. *bioRxiv* 2024.07.02.601742 (2026) doi:10.1101/2024.07.02.601742.
36. Compagnon, V. *et al.* CYP86B1 Is Required for Very Long Chain ω-Hydroxyacid and α,ω-Dicarboxylic Acid Synthesis in Root and Seed Suberin Polyester. *Plant Physiol.* **150**, 1831–1843 (2009).
37. Molina, I., Li-Beisson, Y., Beisson, F., Ohlrogge, J. B. & Pollard, M. Identification of an Arabidopsis Feruloyl-Coenzyme A Transferase Required for Suberin Synthesis. *Plant Physiol.* **151**, 1317–1328 (2009).
38. Belsson, F., Li, Y., Bonaventura, G., Pollard, M. & Ohlrogge, J. B. The Acyltransferase GPAT5 Is Required for the Synthesis of Suberin in Seed Coat and Root of Arabidopsis. *Plant Cell* **19**, 351–368 (2007).
39. Gully, K. *et al.* The GPAT4/6/8 clade functions in Arabidopsis root suberization nonredundantly with the GPAT5/7 clade required for suberin lamellae. *Proc. Natl. Acad. Sci. U. S. A.* **121**, e2314570121 (2024).
40. Mitsuda, N. *et al.* NAC Transcription Factors, NST1 and NST3, Are Key Regulators of the Formation of Secondary Walls in Woody Tissues of Arabidopsis. *Plant Cell* **19**, 270–280 (2007).
41. Geng, P. *et al.* MYB20, MYB42, MYB43, and MYB85 Regulate Phenylalanine and Lignin Biosynthesis during Secondary Cell Wall Formation. *Plant Physiol.* **182**, 1272–1283 (2020).
42. Hsu, F. C. *et al.* Submergence Confers Immunity Mediated by the WRKY22 Transcription Factor in Arabidopsis. *Plant Cell* **25**, 2699–2713 (2013).
43. Hartman, S. *et al.* Ethylene-mediated nitric oxide depletion pre-adapts plants to hypoxia stress. *Nature Communications 2019 10:1* **10**, 4020- (2019).
44. Yang, J. I. *et al.* Increasing Plasma Membrane Phosphatidylinositol(4,5)Bisphosphate Biosynthesis Increases Phosphoinositide Metabolism in Nicotiana tabacum. *Plant Cell* **19**, 1603–1616 (2007).
45. Renna, L., Papini, A., Mancuso, S., Brandizzi, F. & Stefano, G. Plant plastids: from evolutionary origins to functional specialization and organelle interactions. *J. Exp. Bot.* **77**, 63–85 (2025).
46. Enami, K. *et al.* Plastid-to-Nucleus Retrograde Signals Are Essential for the Expression of Nuclear Starch Biosynthesis Genes during Amyloplast Differentiation in Tobacco BY-2 Cultured Cells. *Plant Physiol.* **157**, 518–530 (2011).

47. Carrera, D. Á. *et al.* Distinct plastid fructose bisphosphate aldolases function in photosynthetic and non-photosynthetic metabolism in Arabidopsis. *J. Exp. Bot.* **72**, 3739–3755 (2021).
48. Xu, H. *et al.* Transcriptional networks regulating suberin and lignin in endodermis link development and ABA response. *Plant Physiol.* **190**, 1165–1181 (2022).
49. Ma, F., Jazmin, L. J., Young, J. D. & Allen, D. K. Isotopically nonstationary 13C flux analysis of changes in Arabidopsis thaliana leaf metabolism due to high light acclimation. *Proc. Natl. Acad. Sci. U. S. A.* **111**, 16967–16972 (2014).
50. Xu, Y., Wieloch, T., Kaste, J. A. M., Shachar-Hill, Y. & Sharkey, T. D. Reimport of carbon from cytosolic and vacuolar sugar pools into the Calvin-Benson cycle explains photosynthesis labeling anomalies. *Proc. Natl. Acad. Sci. U. S. A.* **119**, e2121531119 (2022).
51. Kambhampati, S. *et al.* SIMPEL: using stable isotopes to elucidate dynamics of context specific metabolism. *Communications Biology 2024 7:1* **7**, 172- (2024).
52. Ros, R., Muñoz-Bertomeu, J. & Krueger, S. Serine in plants: biosynthesis, metabolism, and functions. *Trends Plant Sci.* **19**, 564–569 (2014).
53. Rosa-Téllez, S. *et al.* The serine–glycine–one-carbon metabolic network orchestrates changes in nitrogen and sulfur metabolism and shapes plant development. *Plant Cell* **36**, 404–426 (2024).
54. Fu, X., Gregory, L. M., Weise, S. E. & Walker, B. J. Integrated flux and pool size analysis in plant central metabolism reveals unique roles of glycine and serine during photorespiration. *Nature Plants 2022 9:1* **9**, 169–178 (2022).
55. Liang, S. *et al.* Identification and Functional Analysis of the Caffeic Acid O-Methyltransferase (COMT) Gene Family in Rice (Oryza sativa L.). *International Journal of Molecular Sciences 2022, Vol. 23,* **23**, (2022).
56. Lloyd, M. K. *et al.* Isotopic clumping in wood as a proxy for photorespiration in trees. *Proc. Natl. Acad. Sci. U. S. A.* **120**, e2306736120 (2023).
57. Morita, K., Hatanaka, T., Misoo, S. & Fukayama, H. Identification and expression analysis of non-photosynthetic Rubisco small subunit, OsRbcS1-like genes in plants. *Plant Gene* **8**, 26–31 (2016).
58. Kelleher, J. K. & Nickol, G. B. Isotopomer Spectral Analysis: Utilizing Nonlinear Models in Isotopic Flux Studies. *Methods Enzymol.* **561**, 303–330 (2015).
59. Schwender, J. & Ohlrogge, J. B. Probing in Vivo Metabolism by Stable Isotope Labeling of Storage Lipids and Proteins in Developing Brassica napusEmbryos. *Plant Physiol.* **130**, 347–361 (2002).
60. Allen, D. K., Shachar-Hill, Y. & Ohlrogge, J. B. Compartment-specific labeling information in 13C metabolic flux analysis of plants. *Phytochemistry* **68**, 2197–2210 (2007).
61. Xu, L., Pan, R. & Zhang, W. Membrane lipids are involved in plant response to oxygen deprivation. *Plant Signalling & Behavior* **15**, (2020).
62. Xie, L. J., Zhou, Y., Chen, Q. F. & Xiao, S. New insights into the role of lipids in plant hypoxia responses. *Prog. Lipid Res.* **81**, 101072 (2021).

63. Kotula, L., Ranathunge, K., Schreiber, L. & Steudle, E. Functional and chemical comparison of apoplastic barriers to radial oxygen loss in roots of rice (Oryza sativa L.) grown in aerated or deoxygenated solution. *J. Exp. Bot.* **60**, 2155–2167 (2009).
64. Andersen, T. G. *et al.* Diffusible repression of cytokinin signalling produces endodermal symmetry and passage cells. *Nature 2018 555:7697* **555**, 529–533 (2018).
65. Ursache, R. *et al.* GDSL-domain proteins have key roles in suberin polymerization and degradation. *Nature Plants 2021 7:3* **7**, 353–364 (2021).
66. Shukla, V. & Barberon, M. Building and breaking of a barrier: Suberin plasticity and function in the endodermis. *Curr. Opin. Plant Biol.* **64**, 102153 (2021).
67. Wessendorf-Rodriguez, K. *et al.* Modeling lipid homeostasis using stable isotope tracing and flux analysis. *Cell Metab.* **38**, 460-473.e6 (2026).
68. Bailey-Serres, J., Geigenberger, P., Perata, P., Sasidharan, R. & Schwarzländer, M. Hypoxia as challenge and opportunity: From cells to crops, to synthetic biology. *Plant Physiol.* **197**, 1–5 (2024).
69. de la Cruz Jiménez, J., Pellegrini, E., Pedersen, O. & Nakazono, M. Radial Oxygen Loss from Plant Roots—Methods. *Plants 2021, Vol. 10,* **10**, (2021).
70. Morcombe, C. R. & Zilm, K. W. Chemical shift referencing in MAS solid state NMR. *Journal of Magnetic Resonance* **162**, 479–486 (2003).
71. Pereira, H. Chemical composition and variability of cork from Quercus suber L. *Wood Sci. Technol.* **22**, 211–218 (1988).
72. Molina, I., Bonaventure, G., Ohlrogge, J. & Pollard, M. The lipid polyester composition of Arabidopsis thaliana and Brassica napus seeds. *Phytochemistry* **67**, 2597–2610 (2006).
73. Del Río, J. C. & Hatcher, P. G. Analysis of aliphatic biopolymers using thermochemolysis with tetramethylammonium hydroxide (TMAH) and gas chromatography–mass spectrometry. *Org. Geochem.* **29**, 1441–1451 (1998).
74. Arumuganathan, K. & Earle, E. D. Nuclear DNA content of some important plant species. *Plant Molecular Biology Reporter 1991 9:3* **9**, 208–218 (1991).
75. Lutz, K. A., Wang, W., Zdepski, A. & Michael, T. P. Isolation and analysis of high quality nuclear DNA with reduced organellar DNA for plant genome sequencing and resequencing. *BMC Biotechnology 2011 11:1* **11**, 54- (2011).
76. Li, H. Minimap2: pairwise alignment for nucleotide sequences. *Bioinformatics* **34**, 3094–3100 (2018).
77. Patro, R., Duggal, G., Love, M. I., Irizarry, R. A. & Kingsford, C. Salmon provides fast and bias-aware quantification of transcript expression. *Nat. Methods* **14**, 417–419 (2017).
78. Robinson, M. D., McCarthy, D. J. & Smyth, G. K. edgeR: a Bioconductor package for differential expression analysis of digital gene expression data. *Bioinformatics* **26**, 139–140 (2010).
79. Camacho, C. *et al.* BLAST+: architecture and applications. *BMC Bioinformatics 2009 10:1* **10**, 421- (2009).

80. Link, V. M. *et al.* Analysis of Genetically Diverse Macrophages Reveals Local and Domain-wide Mechanisms that Control Transcription Factor Binding and Function. *Cell* **173**, 1796-1809.e17 (2018).
81. Michael, T. P. *et al.* High contiguity Arabidopsis thaliana genome assembly with a single nanopore flow cell. *Nature Communications 2018 9:1* **9**, 541- (2018).
82. Li, H. Minimap and miniasm: fast mapping and de novo assembly for noisy long sequences. *Bioinformatics* **32**, 2103–2110 (2016).
83. Wick, R. R., Schultz, M. B., Zobel, J. & Holt, K. E. Bandage: interactive visualization of de novo genome assemblies. *Bioinformatics* **31**, 3350–3352 (2015).
84. Vaser, R., Sović, I., Nagarajan, N. & Šikić, M. Fast and accurate de novo genome assembly from long uncorrected reads. *Genome Res.* **27**, 737–746 (2017).
85. Walker, B. J. *et al.* Pilon: An Integrated Tool for Comprehensive Microbial Variant Detection and Genome Assembly Improvement. *PLoS One* **9**, e112963 (2014).
86. Durand, N. C. *et al.* Juicebox Provides a Visualization System for Hi-C Contact Maps with Unlimited Zoom. *Cell Syst.* **3**, 99–101 (2016).
87. Simão, F. A., Waterhouse, R. M., Ioannidis, P., Kriventseva, E. V. & Zdobnov, E. M. BUSCO: assessing genome assembly and annotation completeness with single-copy orthologs. *Bioinformatics* **31**, 3210–3212 (2015).
88. Benson, G. Tandem repeats finder: a program to analyze DNA sequences. *Nucleic Acids Res.* **27**, 573–580 (1999).
89. Vanburen, R. *et al.* Single-molecule sequencing of the desiccation-tolerant grass Oropetium thomaeum. *Nature 2015 527:7579* **527**, 508–511 (2015).
90. Ou, S. *et al.* Benchmarking transposable element annotation methods for creation of a streamlined, comprehensive pipeline. *Genome Biology 2019 20:1* **20**, 275- (2019).
91. Huerta-Cepas, J. *et al.* Fast Genome-Wide Functional Annotation through Orthology Assignment by eggNOG-Mapper. *Mol. Biol. Evol.* **34**, 2115–2122 (2017).
92. Aylward, A. J., Petrus, S., Mamerto, A., Hartwick, N. T. & Michael, T. P. PanKmer: k-mer-based and reference-free pangenome analysis. *Bioinformatics* **39**, (2023).
93. Emms, D. M. & Kelly, S. OrthoFinder: phylogenetic orthology inference for comparative genomics. *Genome Biology 2019 20:1* **20**, 238- (2019).
94. Emms, D. M., Liu, Y., Belcher, L., Holmes, J. & Kelly, S. OrthoFinder: improved phylogenetic orthology inference with enhanced accuracy and scalability. *Nature Methods 2026 23:7* **23**, 1327–1333 (2026).
95. Buchfink, B., Reuter, K. & Drost, H. G. Sensitive protein alignments at tree-of-life scale using DIAMOND. *Nature Methods 2021 18:4* **18**, 366–368 (2021).
96. Mendes, F. K., Vanderpool, D., Fulton, B. & Hahn, M. W. CAFE 5 models variation in evolutionary rates among gene families. *Bioinformatics* **36**, 5516–5518 (2021).

97. Hartwick, N. T. OrthoPos: Python package and CLI for analysis of orthogroups. Preprint at https://gitlab.com/NolanHartwick/orthopos.
98. Bateman, A. *et al.* UniProt: the Universal Protein Knowledgebase in 2025. *Nucleic Acids Res.* **53**, D609–D617 (2025).
99. Mccleary, B. V *et al.* Measurement of Total Starch in Cereal Products by Amyloglucosidase-α-Amylase Method: Collaborative Study. *J. AOAC Int.* **80**, 571–579 (1997).
100. Antoniewicz, M. R., Kelleher, J. K. & Stephanopoulos, G. Measuring Deuterium Enrichment of Glucose Hydrogen Atoms by Gas Chromatography/Mass Spectrometry. *Anal. Chem.* **83**, 3211–3216 (2011).
101. Hummel, J. *et al.* Ultra performance liquid chromatography and high resolution mass spectrometry for the analysis of plant lipids. *Front. Plant Sci.* **2**, 11588 (2011).
102. Agrawal, S. *et al.* EL-MAVEN: A fast, robust, and user-friendly mass spectrometry data processing engine for metabolomics. *Methods in Molecular Biology* **1978**, 301–321 (2019).
103. Heinrich, P. *et al.* Correcting for natural isotope abundance and tracer impurity in MS-, MS/MS- and high-resolution-multiple-tracer-data from stable isotope labeling experiments with IsoCorrectoR. *Sci. Rep.* **8**, 17910 (2018).
104. Young, J. D. INCA: a computational platform for isotopically non-stationary metabolic flux analysis. *Bioinformatics* **30**, 1333–1335 (2014).

Figures

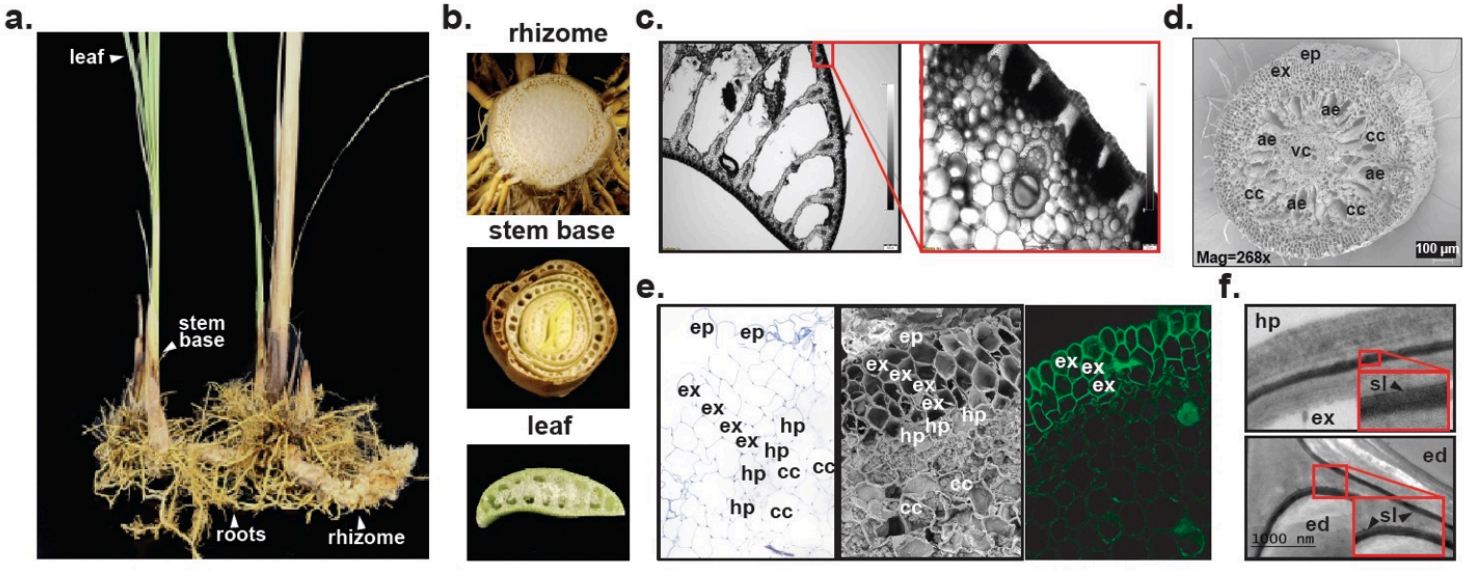


Figure 1

Clonal integration, continuous aeration and selective root barriers in *Typha domingensis*. a, Representative plant showing clonal propagation through interconnected rhizomes linking old and new adjacent shoots. **b,** Transverse sections illustrating extensive aerenchyma in rhizome, stem base and leaf demonstrating the continuity of internal gas spaces from below ground to aerial tissues. **c,** Leaf cross-section showing chlorophyll-containing palisade parenchyma restricted to the outer margins of the blade, with the central region dominated by large lacunae and non-palisade mesophyll. **d,** Scanning electron micrograph (SEM, see Supplemental table S1 for extensive list of abbreviations) of a root cross section at high magnification (268x) **e,** Lugol staining, SEM and Fluorol Yellow staining of root sections showing the multiseriate exodermis highlighted by a strong suberin signal. **f,** Transmission electron micrographs (TEM) showing the light and dark staining of suberin lamellae in both exodermal and endodermal cell walls. Abbreviations: ae, aerenchyma; cc, chlorenchyma/cortical cells; ed, endodermis; ep, epidermis; ex, exodermis; hp, hypodermis; sl, suberin lamellae; vc, vascular cylinder.

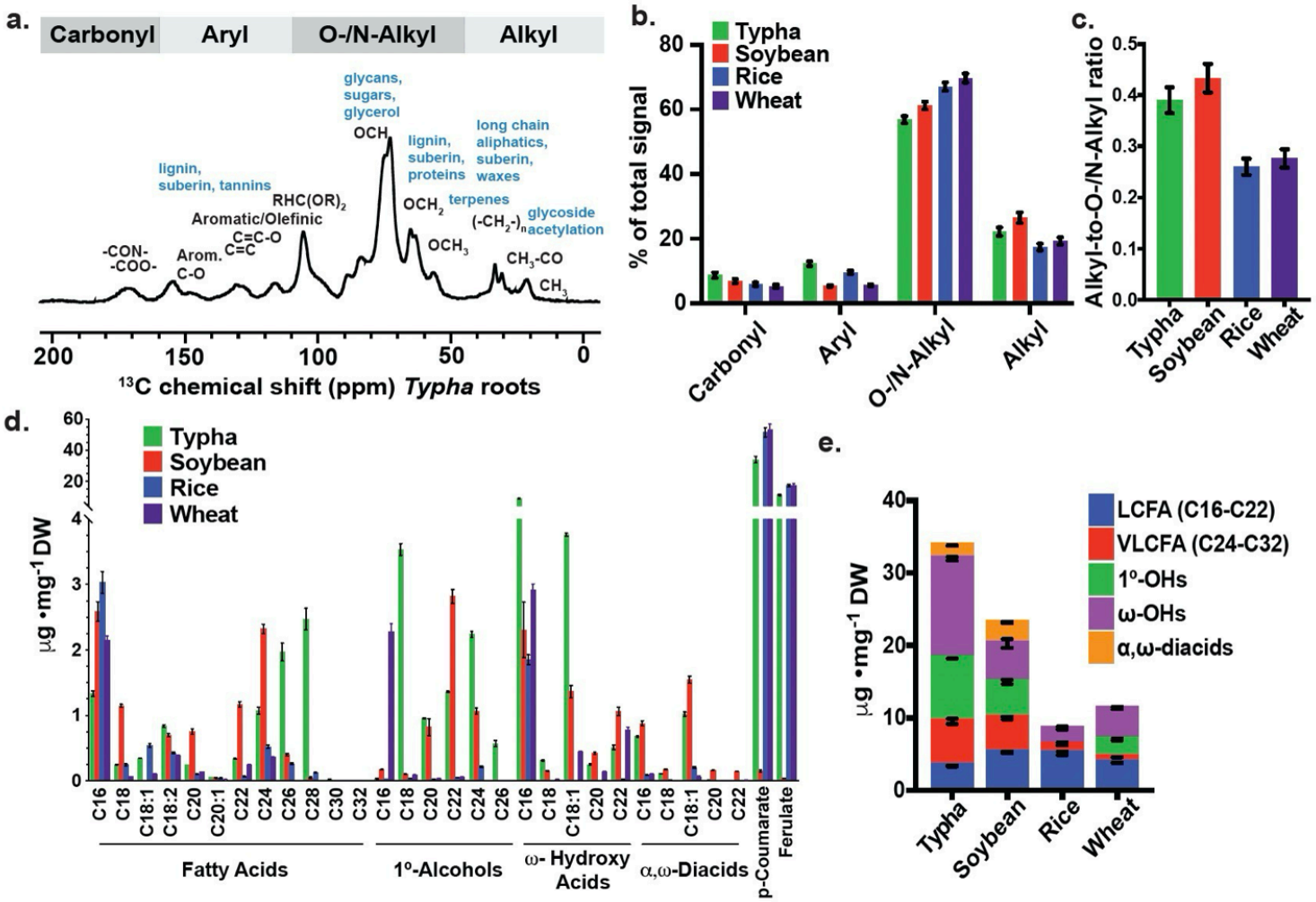


Figure 2

Root cell wall chemistry reveals very-long-chain-rich suberin in *Typha domingensis*. a, Solid-state ^{13}C CP-MAS NMR spectrum of *Typha* roots with the carbonyl, aryl, O-/N-alkyl and alkyl regions highlighted. **b,** Direct-polarization MAS NMR comparison of root carbon distribution in *Typha* (*T. domingensis*), Soybean

(*Glycine max*), Rice (*Oryza sativa*) and Wheat (*Triticum aestivum*). **c,** Alkyl-to-O-/N-alkyl ratios across species. In roots this value is roughly proportional to the fatty acid/polysaccharide ratio. **d,** GC–MS quantification of depolymerized suberin monomers assessing enrichment of very-long-chain fatty acids and hydroxycinnamate-derived aromatics in *Typha*. Error bars represent standard error of mean, n=4 technical replicates. **e,** Summed aliphatic suberin monomer classes across species.

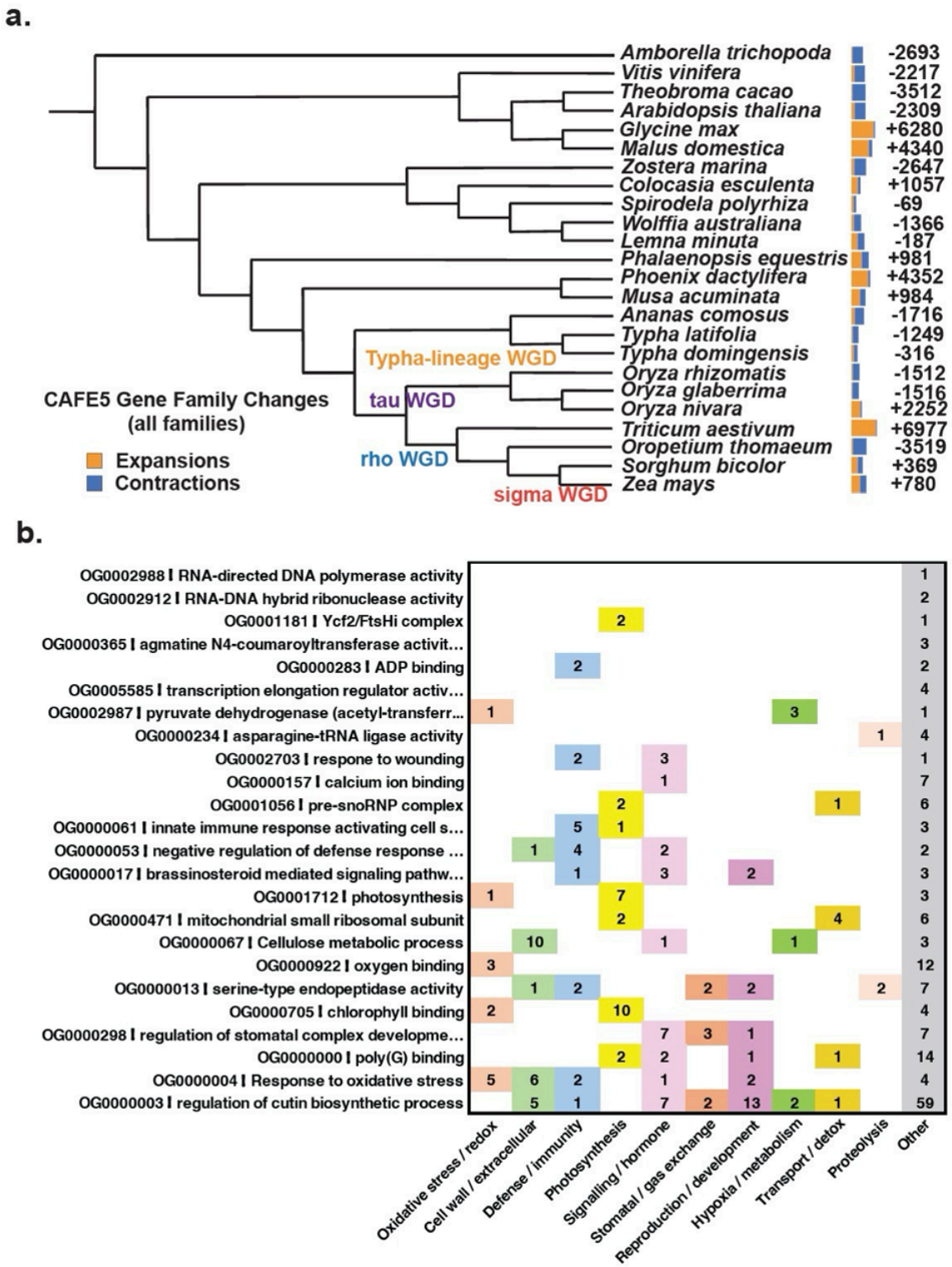


Figure 3

Gene family evolution and functional enrichment across representative angiosperm genomes highlights lineage-specific gene family dynamics in *Typha*. a,Phylogenetic distribution of gene family expansions and contractions inferred using CAFE5 across representative angiosperm species. Orange bars indicate expanded gene families and blue bars indicate contracted gene families relative to inferred ancestral states, with the net gain or loss in gene family number shown beside each species. Major whole-genome duplication (WGD) events (ρ, τ, σ, and the Typha-lineage WGD) are indicated on the phylogeny. **b,** Gene Ontology (GO) enrichment summary of orthogroups significantly expanded in *Typha*spp. relative to rice (*Oryza* spp.). Each row represents an enriched GO term, grouped into broad functional categories shown along the x-axis (oxidative stress/redox, extracellular/cell wall, defense/immunity, photosynthesis, transcription/translation, RNA metabolism, stomatal/gas exchange, reproduction/development, hypoxia/metabolism, transport/ion homeostasis, proteolysis, and other). Colored boxes indicate the functional category assigned to each GO term, and numbers within boxes denote the number of enriched GO terms assigned to that category.

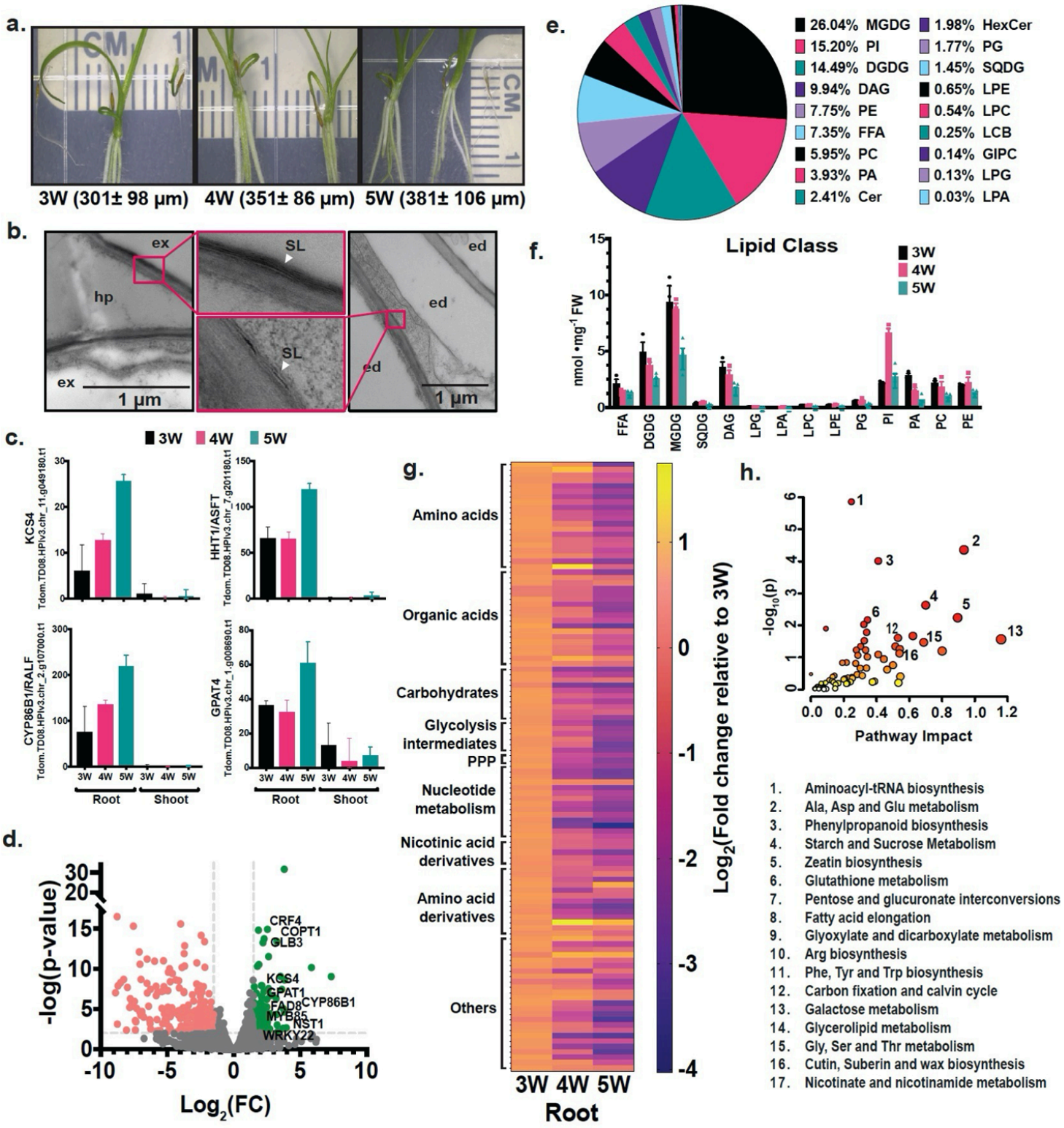


Figure 4

A developmental series captures the onset of suberin deposition in *T. domingensis* roots. a, Sterile plate-grown seedlings harvested at 3, 4 and 5 weeks. **b,** TEMs of 5-week roots showing suberin lamellae in exodermal and endodermal cells. **c,** Expression of representative suberin-associated genes (*KCS4*, *CYP86B1*, *HHT1/ASFT*and *GPAT4*) in roots and shoots across development. Y-axis represents counts per million. **d,** Volcano plot of differentially expressed genes in 5-week versus 3-week roots. **e,** Relative

abundance of lipid classes at 5 weeks. Color code starts with MGDG going clockwise. **f,** Developmental comparison of lipid classes from 3 to 5 weeks. **g,** Heat map of polar metabolites across the developmental series. **h,** Integrated transcript–metabolite pathway analysis identifying phenylpropanoid, carbohydrate, fatty-acid elongation and suberin-associated metabolism as major features of the barrier-forming stage.

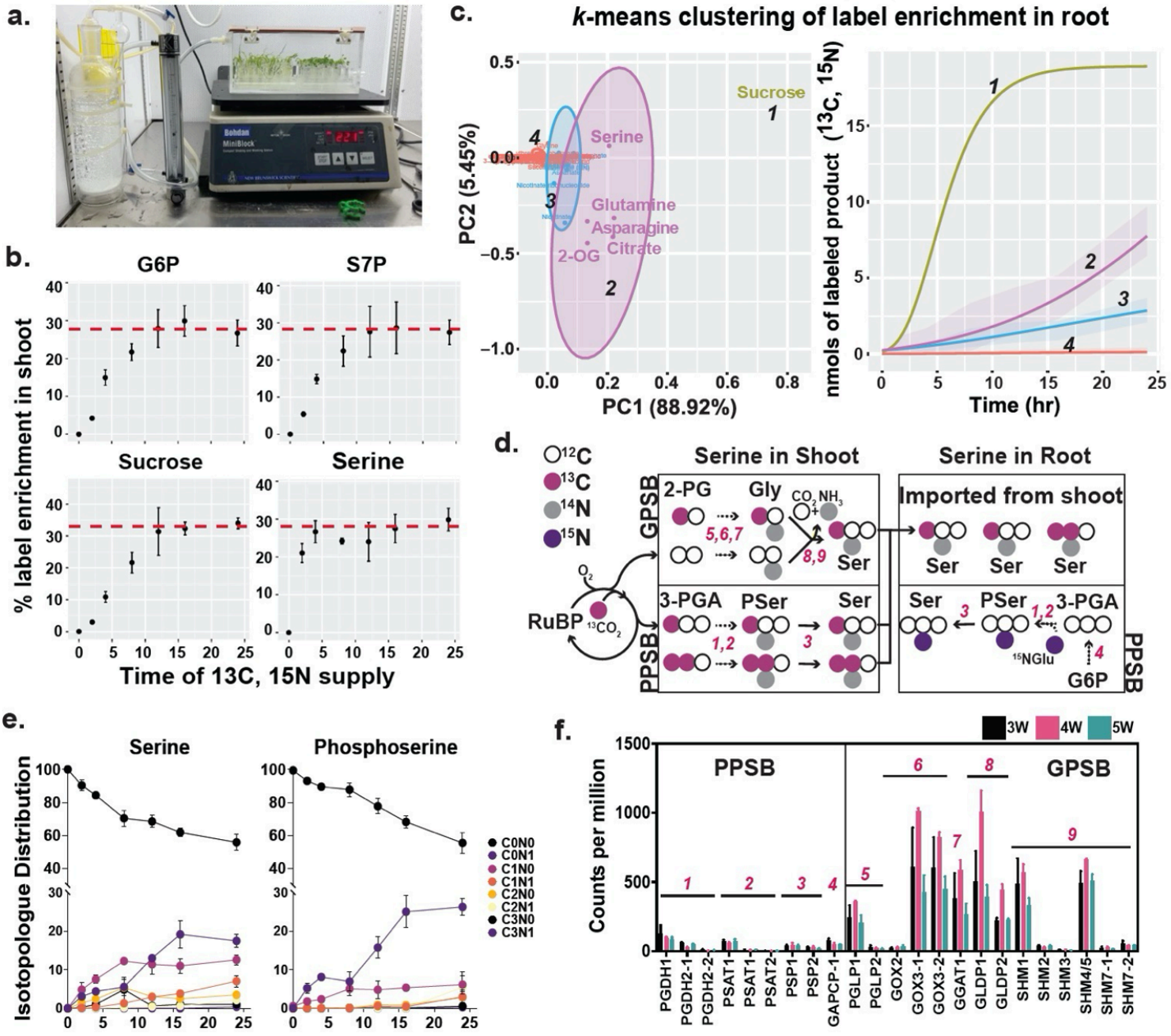


Figure 5

^{13}CO2 tracing identifies shoot-derived carbon sources associated with root suberin formation. a, Image showing set-up for the ^{13}CO2 labelling experiment in 5-week *Typha* seedlings. **b,** Time-resolved enrichment of selected shoot metabolites, including Calvin-cycle intermediates, sucrose and serine. **c,** *k*-

means clustering of root metabolite labelling kinetics identifying sucrose as the fastest-labelled imported carbon source. **d,** Conceptual model for serine labelling through phosphorylated and photorespiratory serine biosynthesis. **e,** Isotopologue distributions of serine and phosphoserine across the time course. **f,** Transcript abundance of genes associated with phosphorylated and glycolate/photorespiratory serine biosynthesis across shoot development.

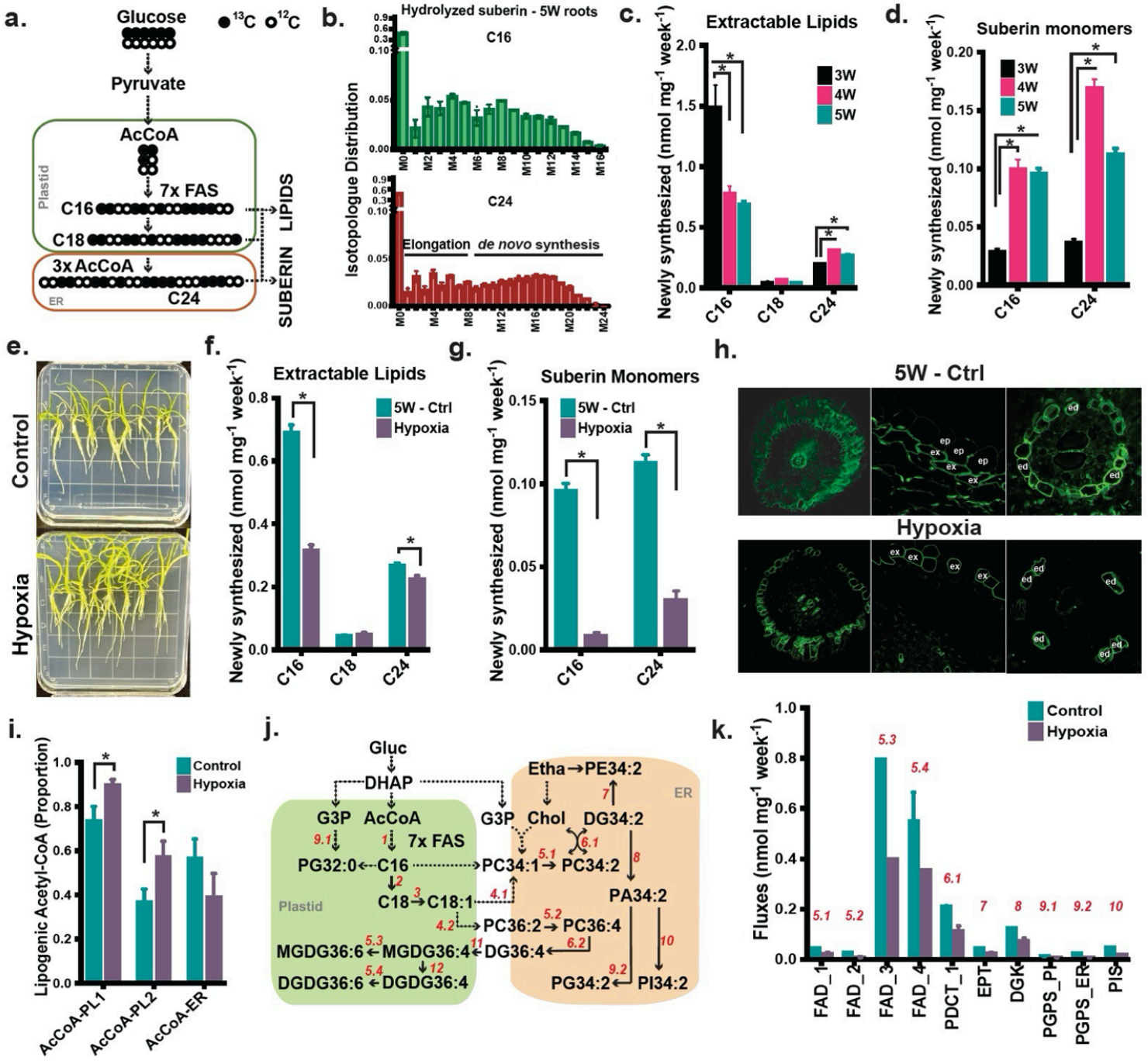


Figure 6

[U-^{13}C]glucose tracing reveals developmental diversion of fatty-acid flux to suberin and selective remodeling under hypoxia. a, Schematic of [U-^{13}C]glucose incorporation into de novo fatty-acid synthesis and elongation. **b,** Representative isotopologue distributions of hydrolyzed suberin monomers

used for isotopomer spectral analysis (ISA). **c,** ISA-derived estimates of newly synthesized extractable lipid fatty acids and **d,** suberin monomers in 3-, 4- and 5-week roots, showing diversion of fatty-acid flux from extractable lipids toward elongation-dependent suberin synthesis during development. Error bars represent upper and lower bounds while significance (*) represents non-overlapping confidence intervals. **e,** Plate growth showing phenotype for 5-week control and hypoxia treatments of *Typha* seedlings. **f,** ISA comparison of extractable lipids and **g,** suberin monomers under control and hypoxia. **h,** Fluorol Yellow staining showing retention of exodermal suberin and reduced endodermal suberin under hypoxia. **i,** Estimated glucose derived lipogenic acetyl-CoA pool contributions. **j,k,** Lipid metabolic flux model and inferred fluxes under control and hypoxia. Numbers in red indicate specific enzymes involved in the reaction and their fluxes as determined by MFA (Supplemental table S22).

Supplementary Files

This is a list of supplementary files associated with this preprint. Click to download.

- Supplementaltables.xlsx
- SupplementalFiguresS16.pdf